

Polarons in two-dimensional atomic crystals

Weng Hong Sio

*Institute of Applied Physics and Materials Engineering,
University of Macau, Macao SAR 999078, P. R. China and
Oden Institute for Computational Engineering and Sciences,
The University of Texas at Austin, Austin, Texas 78712, USA*

Feliciano Giustino*

*Oden Institute for Computational Engineering and Sciences,
The University of Texas at Austin, Austin, Texas 78712, USA and
Department of Physics, The University of Texas at Austin, Austin, Texas 78712, USA*

(Dated: February 17, 2023)

The polaron is the archetypal example of a quasiparticle emerging from the interaction between fermionic and bosonic fields in quantum field theory. In crystalline solids, polarons are formed when electrons and holes become dressed by the quanta of lattice vibrations. While experimental signatures of polarons in bulk three-dimensional materials abound, only rarely have polarons been observed in two-dimensional atomic crystals. Here, we shed light on this asymmetry by developing a quantitative *ab initio* theory of polarons in atomically-thin crystals. Using this conceptual framework, we unravel the real-space structure of the recently-observed hole polaron in hexagonal boron nitride, we discover an unexpected critical condition for the existence of polarons in two-dimensional crystals, and we establish the key materials descriptors and the universal laws that underpin polaron physics in two dimensions.

Polarons in solids are quasiparticle excitations resulting from the interaction between electrons and phonons [1]. Intuitively, polarons can be understood as composite particles where electrons are accompanied by a surrounding distortion of the crystal lattice. In the presence of weak electron-phonon interactions, polarons behave like conventional Bloch waves, only with heavier effective masses. In the presence of strong interactions, on the other hand, polarons become narrow wavepackets and their spatial localization profoundly alters the transport, electrical, and optical properties of the host material [2, 3].

During the last few years, a number of ground-breaking experimental observations of polarons have been made, including in quantum materials [4–7], water-splitting photocatalysts [8–10], photovoltaic perovskites [11–13] and related double perovskites [14]. The common denominator to these studies is that they focus on three-dimensional (3D) bulk materials.

In stark contrast with these observations, direct experimental evidence of polarons in strictly two-dimensional (2D) materials is scarce. Also, from a theoretical standpoint, little is known about polarons in 2D atomic crystals. It is currently unknown whether polarons can form in 2D materials, whether they are localized and to what extent, and how do they respond to external probes. This asymmetry is puzzling when one considers the tremendous progress that the field of 2D materials has seen over the past decade and a half [15, 16]. Two notable exceptions are recent studies of few-layer hexagonal boron nitride (h-BN) on graphene [17], and monolayer molybde-

num disulfide (MoS₂) [18], where mass enhancement and phonon satellites in angle-resolved photoelectron spectra (ARPES) have been observed. It has been proposed that these effects arise from the formation of Fröhlich hole polarons at the h-BN/graphene interfaces, and Holstein polarons in MoS₂. A definitive assignment of the nature of polarons in these systems would require one to probe the real-space structure of the polaron wavefunction or the strain field [12], but this information is currently inaccessible via ARPES which is a momentum-space probe.

Here, we shed light on the nature and existence of polarons in atomically-thin 2D crystals by asking how the energetics and localization of polaron quasiparticles evolves from 3D to 2D, what are the key materials parameters that drive polaron formation in 2D, and why 2D polarons are apparently more difficult to detect than in bulk materials. To answer these questions, we proceed in two steps: first, we focus on h-BN as a case study, and we compute and compare polarons in the bulk crystal and the monolayer. Second, we generalize our findings by developing an exactly-solvable *ab initio*-based model of polarons in 2D materials. This step allows us to examine a broader class of compounds, and to discover hitherto-unknown laws in the physics of polarons in two dimensions.

Our present analysis relies on two recent advances: (i) an *ab initio* computational method for determining polaron formation energies, wavefunctions, and atomic displacements without explicit supercell calculations [19, 20]; (ii) a unified first-principles formulation of long-range polar electron-phonon couplings in 3D and 2D [21]. We express the polaron wavefunction as $\psi(\mathbf{r}) = N^{-1/2} \sum_{n\mathbf{k}} A_{n\mathbf{k}} u_{n\mathbf{k}}(\mathbf{r}) e^{i\mathbf{k}\cdot\mathbf{r}}$, where \mathbf{r} is the position, $u_{n\mathbf{k}}$ is the Bloch-periodic component of a single-particle elec-

* fgiustino@oden.utexas.edu

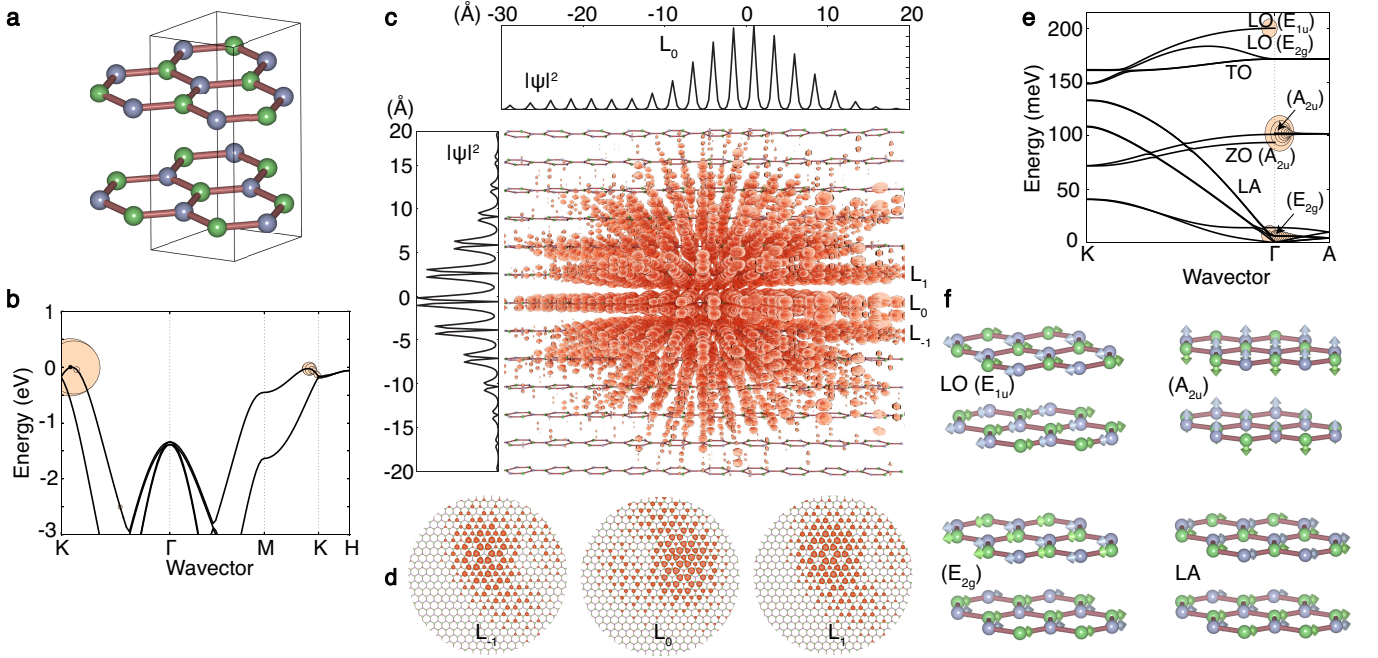


FIG. 1. Large hole polaron in bulk h-BN. (a) Ball-stick model of bulk h-BN with B and N in green and blue, respectively. (b) Valence band structure of bulk h-BN. The Fourier amplitudes of the hole polaron wavefunction are superimposed to the bands as circles with radii proportional to $|A_{n\mathbf{k}}|^2$. (c) Isosurface plot of the hole polaron density $|\psi(\mathbf{r})|^2$ for bulk h-BN for a $24 \times 24 \times 8$ supercell (9216 atoms). An enlarged view of this wavefunction is shown in Supplemental Fig. S2. The left and top panels represent one-dimensional profiles of this density, obtained as the planar average along the c axis (left), and as a slice along a line passing through the center of the polaron (top), respectively. (d) Layer-resolved polaron wavefunction, showing the alternating concentration of charge density from one layer to the next. (e) Phonon dispersion relations of bulk h-BN. The Fourier amplitudes of the polaronic distortion are superimposed to the bands as circles with radii proportional to $|B_{q\nu}|^2$. (f) Atomic displacement patterns of the E_{1u} , A_{2u} , E_{2g} , and LA modes that contribute the most to the polaronic distortion in bulk h-BN.

tron wavefunction for the band n and wavevector \mathbf{k} , and the summation runs over a uniform grid of N points in the Brillouin zone. The coefficients $A_{n\mathbf{k}}$ describe the contribution of the Bloch state $\psi_{n\mathbf{k}}$ to the polaron. Similarly, we express the displacements of the atom κ in the unit cell defined by the lattice vector \mathbf{R} as $\Delta\tau_{\kappa}(\mathbf{R}) = -2N^{-1} \sum_{\mathbf{q}\nu} B_{\mathbf{q}\nu}^* (\hbar/2M_{\kappa}\omega_{\mathbf{q}\nu})^{\frac{1}{2}} \mathbf{e}_{\kappa,\mathbf{q}\nu} e^{i\mathbf{q}\cdot\mathbf{R}}$, where M_{κ} is the atomic mass, $\mathbf{e}_{\kappa,\mathbf{q}\nu}$ is the normal vibrational mode for branch ν and wavevector \mathbf{q} , and $\omega_{\mathbf{q}\nu}$ is the corresponding vibrational frequency. The coefficients $B_{\mathbf{q}\nu}$ provide the contributions of each normal mode to the polaronic lattice distortion. The vectors $A_{n\mathbf{k}}$ and $B_{\mathbf{q}\nu}$ are obtained by solving the *ab initio* polaron equations [19, 20]:

$$\frac{2}{N} \sum_{\mathbf{q}m\nu} B_{\mathbf{q}\nu} g_{m\nu}^*(\mathbf{k}, \mathbf{q}) A_{m\mathbf{k}+\mathbf{q}} = (\varepsilon_{n\mathbf{k}} - \varepsilon) A_{n\mathbf{k}}, \quad (1)$$

$$B_{\mathbf{q}\nu} = \frac{1}{N} \sum_{m\mathbf{k}} A_{m\mathbf{k}+\mathbf{q}}^* \frac{g_{m\nu}(\mathbf{k}, \mathbf{q})}{\hbar\omega_{\mathbf{q}\nu}} A_{n\mathbf{k}}. \quad (2)$$

In these expressions, $\varepsilon_{n\mathbf{k}}$ denotes a single-particle electron eigenvalue, $g_{m\nu}(\mathbf{k}, \mathbf{q})$ is the electron-phonon matrix element connecting the state $\psi_{n\mathbf{k}}$ with the state $\psi_{m\mathbf{k}+\mathbf{q}}$ via the phonon of frequency $\omega_{\mathbf{q}\nu}$ [22], and ε is the polaron eigenvalue. Equations (1) and (2) are solved it-

eratively, and polaron energies are extrapolated to the limit of infinitely-large supercell by densifying the Brillouin zone sampling, as shown in Supplemental Figs. S1-S4. Importantly, this method does not suffer from the self-interaction error of density functional theory, as discussed in Supplemental Note 1. All calculations are performed using Quantum ESPRESSO [23], Wannier90 [24], and EPW [25]. A detailed description of this approach can be found in Ref. [20], and the computational setup including a new formulation of the electron-phonon matrix element in 2D is outlined in the Computational Methods section of the Supplemental Material.

In Fig. 1 we illustrate our results for the hole polaron in bulk h-BN. Figure 1(a) shows the structure of bulk h-BN in the AA' stacking. In this configuration, the B atoms in one layer lie directly above the N atoms in the layer underneath. Figure 1(b) shows the valence bands of bulk h-BN. The top of the bands is near the K point and derives from N- $2p_z$ orbitals. Upon removing one electron and letting the atoms adjust around the hole, a polaron forms as shown in Fig. 1(c). The polaron wavefunction extends over 10 unit cells in the ab plane, and spans 7 atomic layers along the c direction, therefore this is a large hole polaron. Incidentally, we note that performing

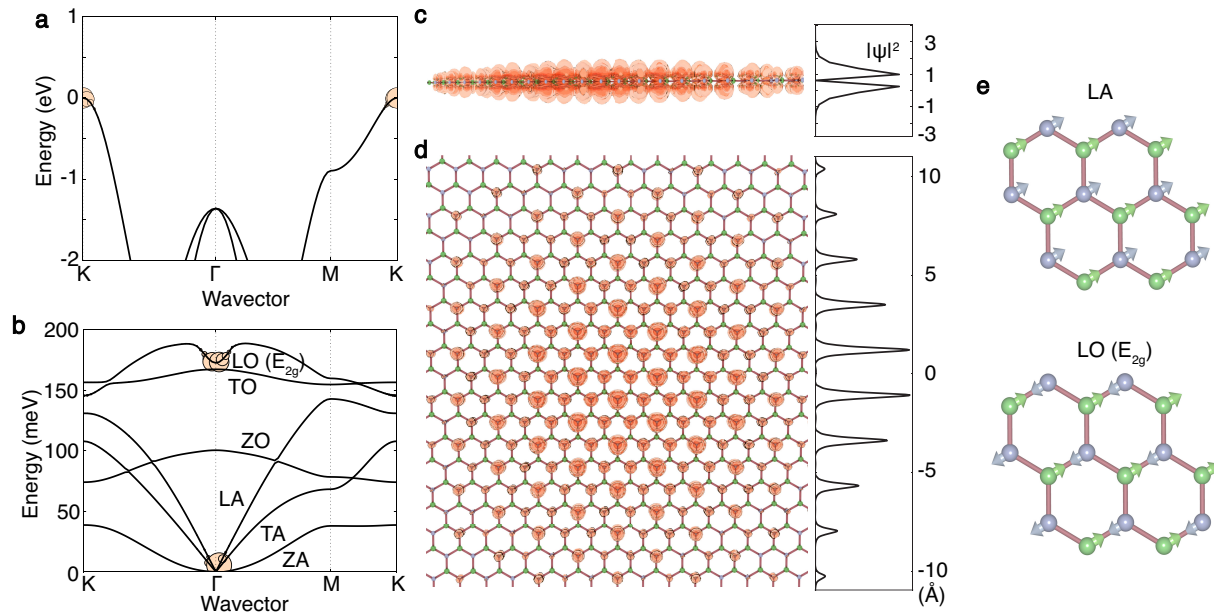


FIG. 2. Fröhlich polaron in monolayer h-BN. (a) Valence band structure of monolayer h-BN. The Fourier amplitudes of the hole polaron wavefunction are superimposed to the bands as circles with radii proportional to $|A_{n\mathbf{k}}|^2$. (b) Phonon dispersion relations of monolayer h-BN. The Fourier amplitudes of the polaronic distortion are superimposed to the bands as circles with radii proportional to $|B_{\mathbf{q}\nu}|^2$. Note that the LO-TO splitting is almost entirely suppressed, as expected from the reduced dimensionality [26]. We see a small residual splitting because the calculations are performed using a large but finite supercell in the c -axis direction, cf. Computational Methods section of the Supplemental Material. (c) Top view of the hole polaron density $|\psi(\mathbf{r})|^2$ for monolayer h-BN for a $26 \times 26 \times 1$ supercell (676 atoms), and one-dimensional profile obtained as the planar average along the axis perpendicular to the monolayer. (d) Side view of the hole polaron density, and one-dimensional profile obtained as a slice along a line passing through the center of the polaron. An enlarged view of this wavefunction is shown in Supplemental Fig. S4. (e) Atomic displacement patterns of the LO E_{2g} and LA modes that provide the dominant contribution to the polaronic distortion in monolayer h-BN.

this calculation without employing the *ab initio* polaron equations Eqs. (1)-(2) would have required supercells of at least 36,000 atoms [Supplemental Fig. S1(a)], which is currently beyond reach using hybrid functionals. Despite the highly anisotropic nature of h-BN, the wavefunction is found to be nearly spherical in shape, with full-width-at-half-maximum of 13 Å along the c axis and 15 Å in the ab plane. This can be seen in the one-dimensional charge density profiles in Fig. 1(c). From the layer-resolved plots in Fig. 1(d), we can also see that the hole density tends to accumulate on opposite sides from one layer to the next. This intriguing pattern originates from the fact that the transverse-optical (TO) E_{2g} interlayer shear mode [Fig. 1(f)] generates macroscopic dipoles with signs alternating between layers, thereby pulling the hole in a zig-zag pattern. The formation energy of this polaron, as measured from the fully-delocalized ground state, is $E = -13.6$ meV, therefore we have a weak polaronic renormalization of the valence band energy.

Figures 1(b) and (e) show the decomposition of the polaron wavefunction and the accompanying atomic displacements into the underlying Bloch states, as obtained by overlaying the coefficients $|A_{n\mathbf{k}}|^2$ and $|B_{\mathbf{q}\nu}|^2$ on the electron and phonon bands. The hole wavefunction derives from the ring of valence band maxima enclosing the

K point [27]. The distribution in reciprocal space is very narrow, consistently with the large size of the wavefunction in real space. Analogous trends have been observed for excitons in h-BN [28–31]. Only long-wavelength phonons are involved in the formation of the polaron, in particular a longitudinal optical (LO) phonon, two TO phonons, and one longitudinal acoustic (LA) phonon. In Fig. 1(f) we see that the LO phonon is an E_{1u} bond-stretching mode propagating in-plane at 201 meV (38%); the TO phonons are the A_{2u} c -axis sliding mode of the B and N sublattices at 102 meV (27%) and the E_{2g} interlayer shear mode at 6 meV (4%), both of which propagate out-of-plane; the LA phonon (31%) is an in-plane compression wave [32]. Since the contributions of LO, TO, and LA phonons are comparable in size, the appropriate classification of polarons in bulk h-BN is as hybrid Fröhlich-Holstein-acoustic polarons. The numerical values provided above will no doubt improve when many-body calculations of electron-phonon matrix elements [22] will become widely available, such as for example the recent GWPT method [33]. However, we expect such improvements to be of the order of 5% or less based on the error analysis reported in Supplemental Note S2.

Next we discuss polarons in monolayer h-BN. The 2D version of h-BN has received considerable attention as

a versatile platform for hyperbolic phonon polaritons [34], single-photon emitters [35], and deep UV emission [36, 37], but the possible role of polarons in these applications is currently unknown. Figure 2(a) shows the band structure of the monolayer, with the top of the valence bands located at the K point of the hexagonal Brillouin zone. Similarly to the case of bulk h-BN, the polaron wavefunctions primarily draws weight from the K valleys. Isosurface plots of the polaron wavefunction are shown in Fig. 2(c) and (d), with views from the side and from the top, respectively, as well as the corresponding one-dimensional profiles. The atomic displacements of this polaron are shown in Supplemental Fig. S3. The wavefunction consists of $N-2p_z$ orbitals modulated by a Gaussian-like envelope, and extends over 9 unit cells with a full-width at half maximum of 10 Å. This wavefunction is more localized than in the case of bulk h-BN, and accordingly the formation energy is higher than in bulk, $E = -15.9$ meV. The structure of the polaron wavefunction is reminiscent of the excitonic wavefunction in monolayer h-BN obtained via the Bethe-Salpeter approach [30]. This similarity reflects the common root of both polarons and excitons in the Coulomb interaction between charged excitations.

Unlike in bulk h-BN, in monolayer h-BN there is no contribution from the interlayer shear mode and from the c -axis sublattice sliding mode, which only exist when more than one layer is present. This is shown in Fig. 2(b). The only vibrational modes contributing to polaron formation are the long-wavelength E_{2g} bond-stretching LO phonon at 172 meV (76%), and the LA phonon (24%). The atomic displacement patterns of these modes are shown in Fig. 2(e). Based on these results, we infer that the polaron in monolayer h-BN is dominated by polar phonon coupling, and therefore it can be classified as a large Fröhlich polaron.

Our present results indicate that the Fröhlich interaction plays an important role both in bulk and in monolayer h-BN. This finding is in line with the recent observation of polaron fingerprints at the interface between few-layer h-BN and graphene [17]. In Ref. 17 ARPES satellites were observed ~ 210 meV below the valence quasi-particle peak. Our calculations support the assignment of these features to polarons with significant Fröhlich character, on the grounds that the LO mode at ~ 200 meV in bulk h-BN [Fig. 1(e)] and its counterpart in monolayer h-BN [Fig. 2(b)] contribute significantly to the formation of the polaron.

If we compare the above results for bulk and monolayer h-BN, we find that the polaron is more stable in the monolayer. This trend is consistent with the observation of stronger exciton binding in van der Waals materials in the monolayer limit [38, 39]. Closer inspection, however, indicates that the analogy between polarons and excitons does not go further: while the exciton binding energy increases by almost an order of magnitude, from 130 meV in bulk h-BN to 0.7 ± 0.2 eV in the monolayer [36, 40, 41], the increase in polaron formation energy is of

only 17% (from 13.6 meV to 15.9 meV). This surprising result calls for a more in-depth analysis. In the following, we investigate how dimensionality determines the nature of polarons by deriving an exactly-solvable model.

For simplicity we focus on the Fröhlich interaction, which dominates the polaron in monolayer h-BN, and we neglect the acoustic phonon contribution. Therefore the following results represent lower bounds to the formation energies. Several studies of Fröhlich polarons in 2D have been reported, shedding light on important aspects of the many-body physics of polarons [42–46]. However, in all this prior work the authors considered 2D sheets without thickness, and this choice leads to unrealistically strong Fröhlich interactions that diverge at long wavelength [45]. Conversely, multiple *ab initio* studies showed that the coupling matrix elements of real 2D crystals are finite at long wavelength [21, 47–49]. Starting from this observation, we use the following expression for the Fröhlich matrix element, which we recently derived from first principles [21]:

$$g(q) = i \left[E_{\text{Ha}} \frac{\pi a_0 d}{2 A} \hbar \omega \epsilon_{\text{ion}} \right]^{1/2} \frac{q_c}{q_c + q}. \quad (3)$$

This matrix element describes the Fröhlich interaction in a homogeneous 2D layer of thickness d and unit cell area A , with a single dispersionless LO phonon of frequency ω . The dielectric screening is uniform and isotropic within this layer, and $\epsilon_{\text{ion}} = \epsilon_0 - \epsilon_\infty$ is the difference between the static relative permittivity ϵ_0 and the high-frequency relative permittivity ϵ_∞ , i.e. the ionic contribution to the dielectric constant. E_{Ha} is the Hartree energy, a_0 the Bohr radius, and q_c is a characteristic wavevector defined by $q_c d = 4\epsilon_\infty / (2\epsilon_\infty^2 - 1)$ [21]. The key difference between Eq. (3) and the standard Fröhlich matrix element in 3D is the presence of q_c at the denominator, which eliminates the characteristic long-wavelength singularity that one encounters in bulk crystals.

Using Eq. (3) inside Eqs. (1)-(2), and considering a single parabolic band with effective mass m^* , we transform the equations into real space to find the polaron formation energy:

$$E = \frac{\hbar^2}{2m^*} \int d\mathbf{r} |\nabla\psi|^2 + \frac{1}{2} \int d\mathbf{r} d\mathbf{r}' |\psi(\mathbf{r})|^2 V_{2\text{D}}(\mathbf{r} - \mathbf{r}') |\psi(\mathbf{r}')|^2, \quad (4)$$

where ψ is the polaron wavefunction and \mathbf{r} is the 2D coordinate. The effective potential $V_{2\text{D}}$ is given by:

$$V_{2\text{D}}(r) = -\frac{1}{2} E_{\text{Ha}} a_0 d q_c^2 \epsilon_{\text{ion}} \phi(q_c r), \quad (5)$$

where $r = |\mathbf{r}|$ and the dimensionless function ϕ is:

$$\phi(s) = s + \frac{\pi}{2} [H_0(s) - Y_0(s)] - \frac{\pi}{2} s [H_1(s) - Y_1(s)]. \quad (6)$$

In this equation, H_0 and H_1 are Struve functions, Y_0 and Y_1 are Bessel functions of the second kind. The derivations of Eq. (4) and Eqs. (5)-(6) are provided in

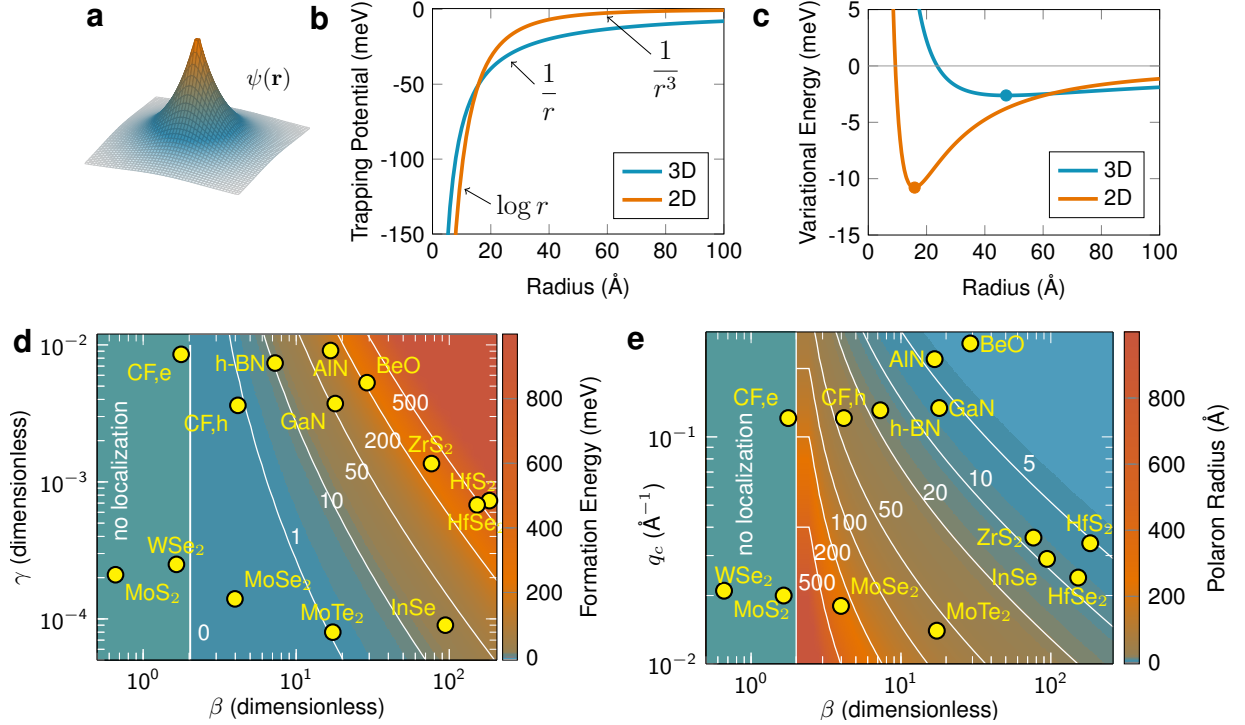


FIG. 3. Continuum model of polarons in two-dimensional atomic crystals. (a) Schematic illustration of the trial variational wavefunction for the 2D Fröhlich polaron model of Eq. (4). (b) Effective polaron self-trapping potentials in three dimensions (cyan) and in two dimensions (orange). For definiteness we use the in-plane dielectric constants of bulk h-BN ($\epsilon_0 = 5.0$ and $\epsilon_\infty = 6.9$), hole effective mass $m^* = 0.65 m_e$ of monolayer h-BN, and set the thickness of the monolayer to the bulk interlayer distance, $d = 3.12 \text{ \AA}$. (c) Energy of polarons in 3D (cyan) and 2D (orange) as a function of the polaron radius r_p . The 3D curve is from the Landau-Pekar model, the 2D curve is from Eq. (7). The dots at the minimum of each curve indicate stable polaron solutions. We employ the same parameters for h-BN as in panel (b). (d) Formation energy map of hole polarons in 2D crystals, as a function of the materials descriptors $\beta = \epsilon_{\text{ion}} m^* d / m_e a_0$, $\gamma = q_c^2 a_0^2 m / m^*$, and $q_c d = 4\epsilon_\infty / (2\epsilon_\infty^2 - 1)$. Polarons do not form when $\beta \leq 2$ (green area). Isolines indicate energies in meV. The yellow disks correspond to hole polarons for the 2D materials reported in Supplemental Table S3. In the case of fluorographene, we report both hole polaron (CF,h) and electron polaron (CF,e). (e) Map of hole polaron radii in 2D crystals, as a function of the materials descriptors β and q_c . The size of the polaron becomes infinite at $\beta = 2$. Isolines indicate radii in \AA . Disks represent the same materials reported in (d).

Supplemental Notes 3 and 4, respectively. The first and second term on the right-hand side of Eq. (4) represent the kinetic energy of the polaron, which favors delocalization; and the potential energy of phonon-mediated self-trapping, which favors localization. Equation (4) can be considered as the generalization of the Landau-Pekar model [50–52] to 2D systems with realistic Fröhlich interactions. In order to highlight similarities and differences between the current model for 2D polarons and the Landau-Pekar model, in Supplemental Table S2 we compare side-by-side the key equations that define these two models.

Figure 3(b) shows the trapping potential V_{2D} . To make contact with our *ab initio* calculations for h-BN, we use the dielectric constants and effective mass of bulk and monolayer h-BN, respectively, and we set the monolayer thickness to the interlayer distance in bulk h-BN. For comparison, in the same figure we plot the corresponding trapping potential in 3D, which has the standard Coulomb form $V_{3D}(r) = -E_{\text{Ha}} a_0 (\epsilon_\infty^{-1} - \epsilon_0^{-1}) / r$ [20, 53].

Unlike in the bulk case, the potential well in 2D is deeper and short-ranged: At short distance ($r \ll q_c^{-1}$) the potential diverges as $\log r$, and at long distance ($r \gg q_c^{-1}$) it behaves as r^{-3} [54]. Equation (6) is reminiscent of the the Rytova-Keldysh potential [55, 56] used in the study of excitons in 2D materials [57], except that it contains additional terms and it is short-ranged.

To analyze the consequences of the short-ranged nature of V_{2D} , we perform a variational calculation of the polaron formation energy. After replacing the hydrogenic ansatz $\psi(\mathbf{r}) = (2/\pi r_p^2)^{1/2} \exp(-|\mathbf{r}|/r_p)$ [20, 51, 53] [cf. Fig. 3(a)] inside Eq. (4), in Supplemental Note 5 we find:

$$E = \frac{\hbar^2}{2m^* r_p^2} - \frac{\epsilon_{\text{ion}}}{4} \frac{e^2 d}{4\pi\epsilon_0 r_p^2} f(q_c r_p). \quad (7)$$

In this expression, the polaron radius r_p serves as the variational parameter, and the dimensionless function f is given in footnote [58]. The two terms on the right-hand side of Eq. (7) correspond to the kinetic and potential energies in Eq. (4), respectively. The competition between

these terms can lead to localized polarons being more stable than delocalized Bloch electrons. Figure 3(c) shows how the energy E depends on the variational parameter r_p for the case of monolayer h-BN. For comparison, we also show the formation energy for bulk h-BN, obtained from the Landau-Pekar model [20, 53]. In agreement with our *ab initio* calculations, the 2D polaron is found to be more stable and more localized than its 3D counterpart. Furthermore, the formation energies obtained from these models, $E = -10.8$ meV for monolayer h-BN and -2.6 meV for bulk h-BN, are in good agreement with our first-principles results. Indeed, since in our *ab initio* calculations the LO modes account for 76% and 38% of the formation energies in monolayer and bulk h-BN, respectively, including only the Fröhlich interaction in these calculations would yield formation energies of -12.1 meV and -5.2 meV, very close to our analytical model.

The modest increase in formation energy from 3D to 2D in h-BN can now be rationalized starting from an analogy with excitons. In the case of excitons, the Coulomb interaction in 2D is stronger than in 3D due to the lack of bulk screening [57]. Extrapolating this reasoning to polarons would lead to the conclusion that formation energies should also increase significantly from 3D to 2D. However, inspection of Eqs. (3) and (7) reveals that polaron formation is driven by the ionic contribution to the dielectric screening ($\epsilon_{\text{ion}} = \epsilon_0 - \epsilon_\infty$), which is significantly reduced in 2D. To see this, let us imagine a bulk system where all layers polarize to trap the electron; if we remove all layers except one, the Coulomb interaction strength between the electron and the surrounding atoms increases due to the reduced screening (as for excitons), however the trapping potential weakens due to the removal of polarizable layers (unlike excitons). These two effects partially compensate, leading to a milder increase of formation energy from 3D to 2D as compared to excitons.

Besides providing us with a compact conceptual framework to interpret detailed *ab initio* calculations, the model of Eq. (7) offers fundamental new insight into the difference between polarons in 2D and 3D. In 3D the self-trapping potential energy goes as r_p^{-1} [20], therefore the interplay between the repulsive kinetic term (which goes as r_p^{-2}) and the attractive Coulomb term always leads to a minimum in the energy landscape. By consequence, in 3D polarons will form no matter how weak the electron-phonon coupling [20, 52, 59–61]. The situation is fundamentally different in 2D. In fact, at large polaron radii, the function f in Eq. (7) becomes a constant [cf. Supplemental Fig. S5], therefore both the attractive and the repulsive terms scale as r_p^{-2} . In this limit, polarons can form only if the prefactor of the attractive term exceeds that of the repulsive term. By requiring this inequality to hold, we obtain a critical condition for the existence of polarons in 2D:

$$\epsilon_{\text{ion}} m^* d > 2 m_e a_0, \quad (8)$$

where m_e is the bare electron mass. One can verify that this condition must also hold for any radius r_p , because the function f in Eq. (7) is monotonic and bound by $f = 1$ from above, as shown in Supplemental Fig. S5. Direct calculations of the formation energy for a broad range of materials parameters, as shown in Fig. 3(d), confirm that 2D polarons do not form when Eq. (8) is not satisfied. As a further test of the validity of this critical condition, we perform explicit *ab initio* calculations of fluorographene, using both the *ab initio* polaron equations Eqs. (1)-(2) and the self-interaction-corrected density-functional approach of Ref. 20. In both cases we do not find stable electron polarons, in agreement with the fact that electrons in fluorographene do not fulfil the critical condition given by Eq. (8). This is seen in Fig. 3(d) and discussed in more detail in Supplemental Note 7 and Supplemental Fig. S3.

The identification of a critical condition for the existence of Fröhlich polarons in 2D marks a significant departure from earlier work. This condition was previously missed because the Fröhlich coupling matrix element employed in prior work [42–46], which describes idealized 2D sheets without thickness, is unrealistically strong and leads to stable polaronic states at all couplings. The use of realistic coupling matrix elements as given by Eq. (3) [21, 47, 48] reveals a more complex picture, where the laws and descriptors previously identified for 3D materials [1] no longer apply. The existence of a critical condition for polaron formation in 2D might explain why there have been far fewer experimental observations of polarons in 2D crystals than in 3D bulk systems.

Figures 3(d) and (e) show how polaron energetics and size vary across the landscape of materials parameters m^* , d , ϵ_∞ , and ϵ_{ion} . The four-dimensional parameters space can be represented via two-dimensional maps by noticing that the formation energy depends only on the dimensionless products $\beta = \epsilon_{\text{ion}} m^* d / m_e a_0$ and $\gamma = a_0^2 m_e q_c^2 / m^*$, while the radius depends only on β and q_c , as discussed in Supplemental Note 6.

Explicit expressions for the formation energy and size of the polaron can be obtained in the weak-coupling limit. In Supplemental Note 6 we show that, in this limit, the energy scales as $\gamma(\beta - 2)^3$, and the polaron radius scales as $[q_c(\beta - 2)]^{-1}$. These scaling laws align with the expectation that strong ionic screening and heavy effective masses, which yield large β values, lead to more stable and more localized polarons. Conversely, when this parameter approaches the critical value $\beta = 2$, the polaron radius diverges and fully-delocalized Bloch states are recovered. The predominant dependence of polaron energy and radius on β (as compared to γ and q_c) suggest that this descriptor should be considered as the 2D counterpart of the Fröhlich coupling constant α that is commonly used for bulk materials [53].

The exactly-solvable model in Eq. (7) is particularly useful to perform a rapid assessment of polaron energetics and size for several 2D materials. In Figs. 3(d) and (e) we include datapoints for popular 2D crystals, namely h-BN,

MoS₂, MoSe₂, MoTe₂, WS₂, WSe₂, HfS₂, HfSe₂, ZrS₂, InSe, as well as fluorographene [62] and the recently-synthesized monolayer h-AlN [63], monolayer h-GaN [64], and monolayer h-BeO [65]. For each compound we determine the descriptors β , γ , and q_c using the materials parameters m^* , d , ϵ_∞ , and ϵ_{ion} from Refs. 21, 48, 66–73, as reported in Supplemental Table S3. For definiteness we focus on hole polarons, and we report the corresponding data for electron polarons in Supplemental Table S3. We immediately see that group-VI transition-metal dichalcogenides (MoS₂, MoSe₂, MoTe₂, WS₂, WSe₂) do not host stable Fröhlich polarons. In particular, MoSe₂ and MoTe₂ fulfill the critical condition in Eq. (8), but the polaron wavefunctions extend over 10-50 nm; it is unlikely that quantum coherence between electron and phonons be maintained over such distances in real, defective crystals. The other group-VI dichalcogenides MoS₂, WS₂, and WS₂ do not satisfy the critical condition in Eq. (8) owing to weak ionic screening, therefore in these cases we do not expect carrier localization. This finding is in agreement with recent work [74] showing that the phonon sidebands observed in ARPES spectra of MoS₂ [18] arise from the coupling of non-polar zone-boundary phonons to delocalized Bloch electrons.

On the other hand, the data for group-IV transition-metal dichalcogenides as well as h-BeO in Figs. 3(d) and (e) paint a very different picture. With polaron sizes in the range of 1-2 nm and formation energies significantly above 100 meV, HfS₂, HfSe₂, ZrS₂, and h-BeO appear to be ideal platforms for investigating strong-coupling polaron physics in two dimensions, as we confirmed by explicit *ab initio* calculations for the cases of ZrS₂ and h-BeO (see Supplemental Note 7 and Supplemental Figs. 2, 4, 9, 10, 12). Group-IV transition-metal dichalcogenide monolayers are rapidly emerging as a promising alternative to group-VI dichalcogenides for field-effect transistors, batteries, thermoelectricity, and catalysis [75], therefore experimental studies of polarons should be within reach. Furthermore, the recent synthesis of h-BeO monolayers by molecular beam epitaxy [65] makes this new material an attractive candidate for flatland electronics owing to its potential for large-scale growth of stable single-crystalline insulators. These emerging materials platforms could be used to test time-resolved strain field mapping of polarons via diffuse X-ray scattering, as recently demonstrated for bulk materials [12], and even to test exotic mechanism of superconductivity such as the bipolaronic pairing scenario [76] in two dimensions.

Beyond these examples, we anticipate that the materials descriptors and the universal laws identified here will serve as a unifying conceptual framework to understand, probe, and control polarons in two-dimensional crystals, and could lead to a step change in our understanding of emergent quasiparticles in low-dimensional materials. In particular, the combination of this framework and these descriptors of polaron behavior with large databases of 2D materials obtained from computational exfoliation of

experimentally known compounds [77] as well as other 2D databases [78] will enable machine learning and AI approaches for deepening our current understanding of polarons in 2D, and possibly open the doors to data-driven design of two-dimensional polaronic materials.

Acknowledgments

This research is primarily supported by the Computational Materials Sciences Program funded by the U.S. Department of Energy, Office of Science, Basic Energy Sciences, under Award No. DE-SC0020129 (software development, theoretical model, *ab initio* calculations). This research used resources of the National Energy Research Scientific Computing Center, a DOE Office of Science User Facility supported by the Office of Science of the U.S. Department of Energy under Contract No. DE-AC02-05CH11231. The authors also acknowledge the Texas Advanced Computing Center (TACC) at The University of Texas at Austin for providing additional HPC resources, including the Frontera and Lonestar6 systems, that have contributed to the research results reported within this paper. URL: <http://www.tacc.utexas.edu>. In the final stage, W.H.S. was supported by the Science and Technology Development Fund of Macau SAR (FDCT) under grant No. 0102/2019/A2 (*ab initio* calculations and data analysis). W.H.S also acknowledges the Information and Communication Technology Office (ICTO) at the University of Macau and the LvLiang Cloud Computing Center of China for providing extra HPC resources, including the High Performance Computing Cluster (HPCC) and TianHe-2 systems.

Supplemental Material for: Polarons in two-dimensional atomic crystals

Contents:

Computational Methods
 Supplemental Notes 1-7
 Supplemental Tables S1-3
 Supplemental Figures S1-S12
 Supplemental References

Computational Methods

All *ab initio* calculations are performed using the Quantum ESPRESSO package [23] (electronic structure and lattice vibrational properties), the wannier90 code [24] (maximally-localized Wannier functions) and the EPW [25] code (interpolation of electron-phonon matrix elements and polarons). We describe h-BN, ZrS₂, fluorographene, and BeO using density functional theory (DFT) in the local density approximation (LDA: bulk h-BN) and the generalized gradient approximation (PBE: monolayer h-BN, ZrS₂, fluorographene and monolayer BeO) [79–81], and we employ ONCV pseudopotentials [82, 83]. In the case of h-BN, we use a planewaves kinetic energy cutoff of 125 Ry. In ground-state calculations and in calculations of phonon frequencies and eigenmodes, we sample the Brillouin zone using a Γ -centered uniform grid of $14 \times 14 \times 6$ points and $12 \times 12 \times 2$ points for bulk and monolayer h-BN, respectively. All lattice vectors and internal coordinates are optimized before proceeding to polaron calculations. We find $a = 2.49$ Å and $c = 6.47$ Å for bulk h-BN, in good agreement with the experimental values $a = 2.50$ Å and $c = 6.65$ [84]. For calculations of monolayer h-BN, we remove one BN layer from the bulk crystal structure, and we increase the c parameter to 80 Å to minimize spurious interactions between periodic replicas [85]. With this choice, monolayer h-BN exhibits a direct band gap at K as expected [37]. The valence bands of monolayer h-BN are relatively insensitive to the size of the vacuum buffer (the choice of vacuum mainly affects the energetics of the interlayer state in the conduction bands at Γ). Our calculated Kohn-Sham band gaps of bulk and monolayer h-BN are $E_g = 4.06$ eV and 4.69 eV, respectively, and agree with previous calculations [86, 87]. In the case of bulk h-BN, we find in-plane and out-of-plane electronic dielectric constants $\epsilon_{\parallel}^{\infty} = 4.85$ and $\epsilon_{\perp}^{\infty} = 2.85$, respectively; and static dielectric constant $\epsilon_{\parallel}^0 = 6.61$ and $\epsilon_{\perp}^0 = 3.39$, respectively. These values are in agreement with previous work [71]. We calculate a hole mass in monolayer h-BN of $0.65 m_e$, in good agreement with previous calculations yielding 0.61 - $0.82 m_e$ [69, 88, 89]. For monolayer ZrS₂, we employ a kinetic energy cutoff of 125 Ry, a uniform and unshifted Brillouin zone grid of $12 \times 12 \times 2$ points for ground-state calculations, and a grid of $12 \times 12 \times 1$ points to compute phonons. The c -axis parameter is set to 60 Å, and the optimized lattice parameter is $a = 3.69$ Å, in good agreement with Ref. 90. In the case of fluorinated graphene (CF), we use a planewaves cutoff of 105 Ry, a wavevector grid of $12 \times 12 \times 1$ points for both ground-state structure and phonon calculations, and $c = 80$ Å. The optimized lattice parameter of monolayer CF is $a = 2.56$ Å, in good agreement with Ref. 91. For monolayer BeO, we employ a cutoff of 125 Ry, a wavevector grid of $12 \times 12 \times 1$ points for both ground-state and phonon calculations, and $c = 80$ Å. The optimized lattice parameter of monolayer BeO is $a = 2.68$ Å, in line with Ref. 65.

Calculations of polarons for monolayer h-BN, ZrS₂, fluorographene, and monolayer BeO are performed using a slab/vacuum superlattice in a supercell geometry. The long-range Fröhlich component of the electron-phonon matrix element is calculated following Ref. 21 as:

$$g_{m\nu}^{\mathcal{L}}(\mathbf{k}, \mathbf{q}) = \frac{e^2}{2\varepsilon_0\Omega} (\hbar/2\omega_{\mathbf{q}\nu})^{1/2} \sum_{\mathbf{G} \neq -\mathbf{q}} \frac{\langle u_{m\mathbf{k}+\mathbf{q}+\mathbf{G}} | u_{n\mathbf{k}} \rangle}{|\mathbf{q}_{\parallel} + \mathbf{G}_{\parallel}|} \sum_{\kappa} M_{\kappa}^{-1/2} e^{-i(\mathbf{q}_{\parallel} + \mathbf{G}_{\parallel}) \cdot \boldsymbol{\tau}_{\kappa\parallel}} \sum_{\alpha\beta} Z_{\kappa,\alpha\beta}^* e_{\kappa\beta,\nu}(\mathbf{q}) \\ \times \left[\delta_{\alpha,\parallel} i(\mathbf{q} + \mathbf{G})_{\alpha} K(\mathbf{q} + \mathbf{G}, \tau_{\kappa z}) - \delta_{\alpha,z} \frac{\partial K(\mathbf{q} + \mathbf{G}, \tau_{\kappa z})}{\partial \tau_{\kappa z}} \right], \quad (\text{S1})$$

where e , ε_0 and Ω are the electron charge, the dielectric permittivity of vacuum, and the supercell volume, respectively. $\omega_{\mathbf{q}\nu}$ is the frequency of a phonon with wavevector \mathbf{q} and branch index ν , and $u_{n\mathbf{k}}$ is the periodic part of the Bloch wavefunction for the wavevector \mathbf{k} and band index n . M_{κ} is the mass of atom κ with equilibrium position $\boldsymbol{\tau}_{\kappa}$ and Born effective charge tensor $Z_{\kappa,\alpha\beta}^*$. $e_{\kappa\beta,\nu}(\mathbf{q})$ indicates the vibrational eigendisplacement, and the \mathbf{G} 's are reciprocal lattice vectors of the supercell. The subscript \parallel indicates in-plane directions, z indicates the out-of-plane direction. The kernel function K appearing in Eq. (S1) is defined as:

$$\begin{aligned}
K(\mathbf{Q}, \tau_z) &= \frac{1}{\rho^- - \rho^+} \frac{1}{Q^2} \\
&\times \left\{ [(\lambda + \rho^- \mu)e^{Q_{\parallel} \tau_z} + (\mu + \rho^- \lambda)e^{-Q_{\parallel} \tau_z}] \times \right. \\
&\times \left[(\lambda + \rho^+ \mu)[e^{(Q_{\parallel} - iQ_z) \tau_z} - e^{-(Q_{\parallel} - iQ_z)d}](Q_{\parallel} + iQ_z) - (\mu + \rho^+ \lambda)[e^{-(Q_{\parallel} + iQ_z) \tau_z} - e^{(Q_{\parallel} + iQ_z)d}](Q_{\parallel} - iQ_z) \right. \\
&+ \frac{\lambda + \rho^+ \mu}{e^{-iQ_z c + \eta} - 1} [1 - e^{-(Q_{\parallel} - iQ_z)d}](Q_{\parallel} + iQ_z) - \frac{\mu + \rho^+ \lambda}{e^{-iQ_z c + \eta} - 1} [1 - e^{(Q_{\parallel} + iQ_z)d}](Q_{\parallel} - iQ_z) \\
&+ \left. \frac{1}{e^{-iQ_z c + \eta} - 1} [e^{(Q_{\parallel} - iQ_z)D} - 1](Q_{\parallel} + iQ_z) - \frac{\rho^+}{e^{-iQ_z c + \eta} - 1} [e^{-(Q_{\parallel} + iQ_z)D} - 1](Q_{\parallel} - iQ_z) \right] \\
&+ [(\lambda + \rho^+ \mu)e^{Q_{\parallel} \tau_z} + (\mu + \rho^+ \lambda)e^{-Q_{\parallel} \tau_z}] \times \\
&\times \left[(\lambda + \rho^- \mu)[1 - e^{(Q_{\parallel} - iQ_z) \tau_z}](Q_{\parallel} + iQ_z) - (\mu + \rho^- \lambda)[1 - e^{-(Q_{\parallel} + iQ_z) \tau_z}](Q_{\parallel} - iQ_z) \right. \\
&+ \frac{\lambda + \rho^- \mu}{e^{iQ_z c + \eta} - 1} [1 - e^{-(Q_{\parallel} - iQ_z)d}](Q_{\parallel} + iQ_z) - \frac{\mu + \rho^- \lambda}{e^{iQ_z c + \eta} - 1} [1 - e^{(Q_{\parallel} + iQ_z)d}](Q_{\parallel} - iQ_z) \\
&+ [e^{(Q_{\parallel} - iQ_z)D} - 1](Q_{\parallel} + iQ_z) - \rho^- [e^{-(Q_{\parallel} + iQ_z)D} - 1](Q_{\parallel} - iQ_z) \\
&+ \left. \frac{1}{e^{iQ_z c + \eta} - 1} [e^{(Q_{\parallel} - iQ_z)D} - 1](Q_{\parallel} + iQ_z) - \frac{\rho^-}{e^{iQ_z c + \eta} - 1} [e^{-(Q_{\parallel} + iQ_z)D} - 1](Q_{\parallel} - iQ_z) \right] \left. \right\}, \tag{S2}
\end{aligned}$$

where the auxiliary quantities λ , μ , ρ^{\pm} , and η appearing in these expressions are defined as follows:

$$\lambda = (1 + 1/\epsilon_{\infty})/2, \tag{S3}$$

$$\mu = (1 - 1/\epsilon_{\infty})/2, \tag{S4}$$

$$\rho^{\pm} = -\frac{e^{Q_{\parallel} D} - e^{\pm \eta} (\lambda e^{-Q_{\parallel} d} + \mu e^{Q_{\parallel} d})}{e^{-Q_{\parallel} D} - e^{\pm \eta} (\mu e^{-Q_{\parallel} d} + \lambda e^{Q_{\parallel} d})}, \tag{S5}$$

$$\eta = \cosh^{-1} \left\{ \cosh[Q_{\parallel} (D - d)] + 2\lambda^2 / (2\lambda - 1) \sinh(Q_{\parallel} D) \sinh(Q_{\parallel} d) \right\}. \tag{S6}$$

In these expressions, ϵ_{∞} is the electronic dielectric permittivity of the 2D layer, d is the size of this layer, D is the size of the vacuum buffer, and $c = d + D$ is the supercell size. ϵ_{∞} and d are defined unambiguously by requiring that the screening in the layer be isotropic, as originally proposed in Ref. 48. To this aim we use Eqs. (64) and (65) of Ref. 21, and we obtain the effective thickness and dielectric constants shown in Supplemental Table S1.

In Ref. 21 it is shown that Eqs. (S1)-(S6) provide the exact long-wavelength limit of the electron-phonon matrix element in polar systems. These expressions reduce to the standard *ab initio* Fröhlich matrix element for bulk 3D systems [92, 93], and to the matrix elements for slabs in vacuum with Coulomb truncation for isolated 2D systems [48]. The matrix element in Eq. (3) of the main text was derived in Ref. 21 starting from Eqs. (S1)-(S6). In our *ab initio* calculations, we use $g^{\mathcal{L}}$ in conjunction with Wannier-Fourier interpolation [94], as described in Refs. 21 and 92. To perform these calculations, we employ a supercell of size $c = 80 \text{ \AA}$. We checked that the polaron formation energy is well-converged with this vacuum buffer. Using $c = 80 \text{ \AA}$ we obtain a very small LO-TO splitting in monolayer h-BN, $\Delta \hbar \omega = 5 \text{ meV}$. This is consistent with the expectation that the splitting vanishes in the limit of infinite supercell size [26]. To correctly describe a single polaron in the entire crystal, we take the limit of infinite supercell in the in-plane direction. Figure S1(a) shows the formation energy of polarons in bulk h-BN for supercell sizes ranging from $30 \times 30 \times 10$ to $84 \times 84 \times 28$. Figure S1(b) reports the corresponding data for monolayer h-BN, with supercell sizes ranging from $42 \times 42 \times 1$ to $152 \times 152 \times 1$. The corresponding plots for monolayer ZrS₂, CF, and BeO are shown in Figs. S2, S3, and S4, respectively.

We note that the *ab initio* polaron equations, Eqs. (1)-(2) of the main text, provide a lower bound to the polaron formation energy. In the case of 3D systems, the formation energy given by Eqs. (1)-(2) is typically very accurate at strong coupling, and tends to underestimate the exact many-body energy at weak coupling. This behavior is discussed in detail in Refs. 95 and 96.

Supplemental Note 1: Analysis of self-interaction error

In this Note we discuss the impact of the self-interaction error in DFT calculations of polarons. To keep the analysis as simple as possible, we consider the Landau-Pekar model of polarons in 3D, see for example Refs. 20 and 52. This model describes an excess electron in a dielectric continuum, whose energy is given by:

$$E_{\text{LP}} = \frac{\hbar^2}{2m^*} \int d\mathbf{r} |\nabla\psi(\mathbf{r})|^2 - \frac{e^2}{4\pi\epsilon_0} \left(\frac{1}{\epsilon_\infty} - \frac{1}{\epsilon_0} \right) \int d\mathbf{r}' \frac{|\psi(\mathbf{r}')|^2}{|\mathbf{r} - \mathbf{r}'|}. \quad (\text{S7})$$

Here, ψ is the electron wavefunction and all other quantities are defined in the main text. If we were to study this model within DFT, the electron would experience self-interaction. Considering only the Hartree self-interaction for simplicity, the above energy would be modified as:

$$E_{\text{SI}} = E_{\text{LP}} + \frac{e^2}{4\pi\epsilon_0} \int d\mathbf{r}' \frac{|\psi(\mathbf{r}')|^2}{|\mathbf{r} - \mathbf{r}'|}. \quad (\text{S8})$$

The Hartree self-interaction term and the electron-lattice attraction share the same integral, therefore their prefactors can be combined as follows:

$$E_{\text{SI}} = \frac{\hbar^2}{2m^*} \int d\mathbf{r} |\nabla\psi(\mathbf{r})|^2 + \frac{e^2}{4\pi\epsilon_0} \left(1 - \frac{1}{\epsilon_\infty} + \frac{1}{\epsilon_0} \right) \int d\mathbf{r}' \frac{|\psi(\mathbf{r}')|^2}{|\mathbf{r} - \mathbf{r}'|}. \quad (\text{S9})$$

Since $\epsilon_0 \geq \epsilon_\infty \geq 1$ for all materials, the quantity $(1 - 1/\epsilon_\infty + 1/\epsilon_0)$ belongs to the interval $[0, 1]$, hence the potential energy is repulsive. As a result, the energy minimum is achieved for a fully-delocalized electron, and self-interaction has completely suppressed the formation of the polaron.

Hubbard-corrected DFT and hybrid-functional DFT mitigate the self-interaction error of DFT, but do not remove it completely. To see this, we rewrite Eq. (S9) by adding an exchange term as in hybrid-functional DFT:

$$E_{\text{Hy}} = E_{\text{SI}} - \alpha \frac{e^2}{4\pi\epsilon_0} \int d\mathbf{r}' \frac{|\psi(\mathbf{r}')|^2}{|\mathbf{r} - \mathbf{r}'|}, \quad (\text{S10})$$

where α is the fraction of exact exchange in the hybrid functional. With this correction term, polaron localization does not occur for $\alpha < \alpha_c$, where the critical fraction of exact exchange is $\alpha_c = 1 - 1/\epsilon_\infty + 1/\epsilon_0$. For $\alpha > \alpha_c$, a polaron forms, but its formation energy increases quadratically with α , $E_{\text{Hy}} = -\text{const} \cdot (\alpha - \alpha_c)^2$. These trends are a manifestation of residual self-interaction.

This analysis is consistent with the hybrid functional calculations of Ref. 97: in that work the authors find small polarons in MgO only for $\alpha > 0.48$, and the polaron formation energy increases with α beyond this critical value. Our present estimate (with $\epsilon_\infty = 2.4$ and $\epsilon_0 = 9.8$ for MgO), yields $\alpha_c = 0.68$, which is in good agreement with Ref. 97 considering that our estimate refers to the limit of infinite supercell, whereas the calculation of Ref. 97 is for a $3 \times 3 \times 3$ supercell.

Unlike DFT, Hubbard-corrected DFT, and hybrid-functional DFT, the self-interaction error is not present in Eqs. (1)-(2) of the main text, since these equations were derived in Ref. 20 starting from a self-interaction-corrected functional.

Supplemental Note 2: Uncertainty quantification for h-BN

The calculations for bulk h-BN presented in this manuscript employ band structures, phonon dispersions, and electron-phonon matrix elements obtained from DFT/LDA. We expect that the use of non-local functionals such as hybrid functionals or the recently-developed GW perturbation theory (GWPT) [98] will modify the polaron formation energy to some extent, but it will not affect our conclusions, as shown in the following.

Hybrid-functional calculations or GWPT are currently beyond reach for the system under consideration, which requires a supercell with 36,000 atoms. Nevertheless, we can estimate the correction to the formation energy using the 3D Landau-Pekar model introduced in Supplemental Note 1 and discussed in more detail in Supplemental Note 5 [20, 52]. In this model, the formation energy of the polaron scales with the 3D Fröhlich coupling constant α_{F} [52]:

$$\alpha_{\text{F}} = \frac{e^2}{4\pi\epsilon_0\hbar} \left(\frac{1}{\epsilon_\infty} - \frac{1}{\epsilon_0} \right) \sqrt{\frac{m^*}{2\hbar\omega_{\text{LO}}}}. \quad (\text{S11})$$

The materials parameters entering this expression are the effective mass m^* , the frequency of longitudinal-optical phonons ω_{LO} , the high-frequency dielectric constant ϵ_∞ , and the static dielectric constant ϵ_0 . Our DFT/LDA calculations yield the following values:

$$m^* = 0.54 m_e, \quad \omega_{\text{LO}} = 201 \text{ meV}, \quad \epsilon_\infty = 4.85, \quad \epsilon_0 = 6.61.$$

Using these values in Eq. (S11), we obtain $\alpha_F = 0.331$. If we evaluate instead the coupling constant using experimental values for the same parameters, namely the effective mass from Ref. 99 and all other parameters from Ref. 100:

$$m^* = 0.49 m_e, \quad \omega_{LO} = 200 \text{ meV}, \quad \varepsilon_\infty = 4.95, \quad \varepsilon_0 = 6.85,$$

we obtain $\alpha_F^{\text{exp}} = 0.323$. This value is within 3% of our DFT/LDA result, therefore we expect a negligible change in the polaron formation energy. In fact, in the weak-coupling limit, the energy is given by $\alpha_F \hbar \omega_{LO}$, while in the strong coupling limit it is given by $\alpha_F^2 \hbar \omega_{LO} / 3\pi$ [52]. In either case, the corrected energy is within 5% of our original result, thus supporting our initial choice of using DFT/LDA for h-BN.

Supplemental Note 3: Derivation of Eq. (4) of the main text

In this Note we outline the key steps of the derivation of the polaron formation energy in two dimensions, as given in Eq. (5) of the main text. We refer to Ref. [19, 20] for a derivation of the *ab initio* polaron equations, Eqs. (2) and (3) of the main text.

We begin by rewriting Eqs. (2) and (3) of the main text for the case of a single parabolic electron band with effective mass m^* , and a single dispersionless longitudinal optical phonon with frequency ω (the discussion of holes leads to the same results):

$$\frac{2}{\Omega_{\text{BZ}}} \int_{\text{BZ}} d\mathbf{q} B_{\mathbf{q}} g_{\mathbf{q}}^* A_{\mathbf{k}+\mathbf{q}} = (\varepsilon_{\mathbf{k}} - \varepsilon) A_{\mathbf{k}}, \quad (\text{S12})$$

$$B_{\mathbf{q}} = \frac{g_{\mathbf{q}}}{\hbar\omega} \frac{1}{\Omega_{\text{BZ}}} \int_{\text{BZ}} d\mathbf{k} A_{\mathbf{k}+\mathbf{q}}^* A_{\mathbf{k}}. \quad (\text{S13})$$

In these expressions, \mathbf{k} and \mathbf{q} are electron and phonon wavevectors, respectively, $g_{\mathbf{q}}$ is the Fröhlich matrix element, Ω_{BZ} is the volume of the Brillouin zone, and the limit of dense Brillouin zone sampling has been taken. $A_{\mathbf{k}}$ and $B_{\mathbf{q}}$ are the amplitudes of the polaron wavefunctions and associated normal mode coordinates, and ε is the polaron energy eigenvalue. The electron bands are given by $\varepsilon_{\mathbf{k}} = \hbar^2 |\mathbf{k}|^2 / 2m^*$. These expressions are for a standard three-dimensional (3D) bulk crystal, as in Ref. [19, 20].

Using the same assumptions of single band and single LO phonon, the formation energy of the polaron given in Eq. (42) of Ref. [20] can be written as follows:

$$E = \varepsilon + \hbar\omega \int_{\text{BZ}} \frac{d\mathbf{q}}{\Omega_{\text{BZ}}} |B_{\mathbf{q}}|^2, \quad (\text{S14})$$

where we have taken the zero of the energy to coincide with the conduction band bottom. By combining Eqs. (S12)-(S14) we obtain:

$$E = \frac{1}{\Omega_{\text{BZ}}} \int_{\text{BZ}} d\mathbf{k} \varepsilon_{\mathbf{k}} |A_{\mathbf{k}}|^2 - \frac{1}{\hbar\omega} \int_{\text{BZ}} \frac{d\mathbf{q}}{\Omega_{\text{BZ}}} |g_{\mathbf{q}}|^2 |f_{\mathbf{q}}|^2, \quad (\text{S15})$$

where we have used the normalization of the polaron amplitudes [20]:

$$\frac{1}{\Omega_{\text{BZ}}} \int_{\text{BZ}} d\mathbf{k} |A_{\mathbf{k}}|^2 = 1, \quad (\text{S16})$$

and we have introduced the auxiliary function:

$$f_{\mathbf{q}} = \frac{1}{\Omega_{\text{BZ}}} \int_{\text{BZ}} d\mathbf{k} A_{\mathbf{k}+\mathbf{q}}^* A_{\mathbf{k}}. \quad (\text{S17})$$

The polaron wavefunction is given by Eq. (33) of Ref. [20], which we rewrite here as:

$$\psi(\mathbf{r}) = \frac{1}{\Omega_{\text{BZ}}} \int_{\text{BZ}} d\mathbf{k} A_{\mathbf{k}} u_{\mathbf{k}}(\mathbf{r}) e^{i\mathbf{k}\cdot\mathbf{r}}. \quad (\text{S18})$$

In this expression, $u_{\mathbf{k}}$ is the Bloch-periodic component of the wavefunction, and \mathbf{r} is the position vector in 3D. We now specialize to the case of a 2D material of thickness d , contained in an otherwise empty supercell of size L . We describe the confinement of the electronic states in the slab using a simple square function:

$$u_{\mathbf{k}}(\mathbf{r}) = \begin{cases} (Ad)^{-1/2} & 0 < z < d \\ 0 & d < z < L \end{cases}, \quad (\text{S19})$$

where A is the area of the unit cell in the plane of the slab. Other choices for the profile of the wavefunction along the z axis lead to the same results in the limit $L \gg d$. When we take the limit $L \gg d$, the Brillouin zone size along the z axis tends to vanish, therefore $A_{\mathbf{k}}$ can be replaced by $A_{k_x, k_y, 0}$. We will indicate this quantity as $A_{\mathbf{k}_{\parallel}}$. Similarly we will use \mathbf{r}_{\parallel} to indicate the in-plane position vector, and $\Omega_{\text{BZ}_{\parallel}} = (2\pi)^2/A$ to denote the 2D Brillouin zone. With the choice made in Eq. (S19), the wavefunction in Eq. (S18) can be rewritten as:

$$\psi(\mathbf{r}) = \int_{\text{BZ}_{\parallel}} \frac{d\mathbf{k}_{\parallel}}{\Omega_{\text{BZ}_{\parallel}}} A_{\mathbf{k}_{\parallel}} e^{i\mathbf{k}_{\parallel} \cdot \mathbf{r}_{\parallel}} \times \begin{cases} (Ad)^{-1/2} \text{sinc}(\pi z/L) e^{i\pi z/L} & 0 < z < d \\ 0 & d < z < L \end{cases}. \quad (\text{S20})$$

In the limit $L \gg d$, the terms dependent on z approach unity as z is bound by d , therefore the last expression simplifies to:

$$\psi(\mathbf{r}_{\parallel}, z) = \frac{1}{\sqrt{A}} \int_{\text{BZ}_{\parallel}} \frac{d\mathbf{k}_{\parallel}}{\Omega_{\text{BZ}_{\parallel}}} A_{\mathbf{k}_{\parallel}} e^{i\mathbf{k}_{\parallel} \cdot \mathbf{r}_{\parallel}} \times \begin{cases} 1/\sqrt{d} & 0 < z < d \\ 0 & d < z < L \end{cases}. \quad (\text{S21})$$

Let us call $\phi(\mathbf{r}_{\parallel})$ the first term in the product on the right-hand side of the last equation. We have:

$$\phi(\mathbf{r}_{\parallel}) = \frac{1}{\sqrt{A}} \int_{\text{BZ}_{\parallel}} \frac{d\mathbf{k}_{\parallel}}{\Omega_{\text{BZ}_{\parallel}}} A_{\mathbf{k}_{\parallel}} e^{i\mathbf{k}_{\parallel} \cdot \mathbf{r}_{\parallel}}. \quad (\text{S22})$$

This relation can be inverted to obtain $A_{\mathbf{k}_{\parallel}}$ in terms of $\phi(\mathbf{r}_{\parallel})$:

$$A_{\mathbf{k}_{\parallel}} = \frac{1}{\sqrt{A}} \int d\mathbf{r}_{\parallel} e^{-i\mathbf{k}_{\parallel} \cdot \mathbf{r}_{\parallel}} \phi(\mathbf{r}_{\parallel}). \quad (\text{S23})$$

We now replace this expression inside Eq. (S17). After using Eq. (S22) we find:

$$f_{\mathbf{q}} = \int d\mathbf{r}_{\parallel} e^{i\mathbf{q} \cdot \mathbf{r}_{\parallel}} |\phi(\mathbf{r}_{\parallel})|^2. \quad (\text{S24})$$

Using this result, the second term on the right-hand side of Eq. (S15) becomes:

$$-\frac{1}{\hbar\omega} \int_{\text{BZ}} \frac{d\mathbf{q}}{\Omega_{\text{BZ}}} |g_{\mathbf{q}}|^2 |f_{\mathbf{q}}|^2 = \frac{1}{2} \int d\mathbf{r}_{\parallel} d\mathbf{r}'_{\parallel} |\phi(\mathbf{r}_{\parallel})|^2 V_{2\text{D}}(\mathbf{r}_{\parallel} - \mathbf{r}'_{\parallel}) |\phi(\mathbf{r}'_{\parallel})|^2, \quad (\text{S25})$$

having defined:

$$V_{2\text{D}}(\mathbf{r}_{\parallel}) = -\frac{2}{\hbar\omega} \int_{\text{BZ}_{\parallel}} \frac{d\mathbf{q}_{\parallel}}{\Omega_{\text{BZ}_{\parallel}}} e^{i\mathbf{q}_{\parallel} \cdot \mathbf{r}_{\parallel}} |g_{\mathbf{q}}|^2. \quad (\text{S26})$$

The first term on the right-hand side of Eq. (S15) can be obtained along similar steps. First, we replace the expression for $A_{\mathbf{k}}$ from Eq. (S23):

$$\frac{1}{\Omega_{\text{BZ}}} \int_{\text{BZ}} d\mathbf{k} \epsilon_{\mathbf{k}} |A_{\mathbf{k}}|^2 = \frac{1}{\sqrt{A}} \int d\mathbf{r}_{\parallel} \phi(\mathbf{r}_{\parallel}) \int_{\text{BZ}_{\parallel}} \frac{d\mathbf{k}_{\parallel}}{\Omega_{\text{BZ}_{\parallel}}} A_{\mathbf{k}}^* \frac{\hbar^2 |\mathbf{k}|^2}{2m^*} e^{-i\mathbf{k} \cdot \mathbf{r}_{\parallel}}. \quad (\text{S27})$$

Then, we rewrite the Brillouin-zone integral on the right using the real-space kinetic energy operator, and we substitute Eq. (S22):

$$\frac{1}{\Omega_{\text{BZ}}} \int_{\text{BZ}} d\mathbf{k} \epsilon_{\mathbf{k}} |A_{\mathbf{k}}|^2 = - \int d\mathbf{r}_{\parallel} \phi(\mathbf{r}_{\parallel}) \frac{\hbar^2 \nabla^2}{2m^*} \phi^*(\mathbf{r}_{\parallel}). \quad (\text{S28})$$

By combining Eqs. (S28) and (S25) inside Eq. (S15), we obtain Eq. (4) of the main text.

Supplemental Note 4: Derivation of Eqs. (5) and (6) of the main text

In this Note we derive the effective self-trapping potential $V_{2\text{D}}$ in Eqs. (5) and (6) of the main text. To this end, we consider the expression for the Fröhlich matrix element in 2D as derived in Eq. (62) of Ref. [21], and reproduced in the main text as Eq. (3):

$$g(q) = \sqrt{E_{\text{Ha}} \frac{\pi a_0 d}{2 A} \hbar\omega \epsilon_{\text{ion}} \frac{q_c}{q_c + q}}. \quad (\text{S29})$$

In this expression, $q = |\mathbf{q}_{\parallel}|$, E_{Ha} is the Hartree energy, a_0 is the Bohr radius, and ϵ_{ion} is the ionic contribution to the dielectric permittivity. q_c is a characteristic wavevector defined in the main text. We replace Eq. (S29) inside Eq. (S26) to obtain:

$$V_{2\text{D}}(\mathbf{r}_{\parallel}) = -E_{\text{Ha}} \frac{\pi a_0 d}{(2\pi)^2} \epsilon_{\text{ion}} q_c^2 \int_{\text{BZ}_{\parallel}} \frac{e^{i\mathbf{q}\cdot\mathbf{r}_{\parallel}} d\mathbf{q}_{\parallel}}{(q_c + q)^2}. \quad (\text{S30})$$

The integral can be carried out in cylindrical coordinates, after replacing the Brillouin zone area by an equivalent disk of radius $\pi q_{\text{BZ}_{\parallel}}^2 = \Omega_{\text{BZ}_{\parallel}}$:

$$V_{2\text{D}}(\mathbf{r}_{\parallel}) = -E_{\text{Ha}} \frac{\pi a_0 d}{(2\pi)^2} \epsilon_{\text{ion}} q_c^2 \int_0^{q_{\text{BZ}_{\parallel}}} \frac{q dq}{(q_c + q)^2} \int_0^{2\pi} d\theta e^{iqr \cos \theta}. \quad (\text{S31})$$

In this expression, $r = |\mathbf{r}_{\parallel}|$. The angular integral on the right is $2\pi J_0(qr)$, with J_0 denoting the Bessel function of the first kind. Therefore we have:

$$V_{2\text{D}}(\mathbf{r}_{\parallel}) = -E_{\text{Ha}} \frac{a_0 d}{2} \epsilon_{\text{ion}} q_c^2 \int_0^{q_{\text{BZ}_{\parallel}} r} \frac{x J_0(x) dx}{(q_c r + x)^2}. \quad (\text{S32})$$

The integration bound can be extended to infinity without making a significant error, as it is usually done for the Fröhlich model in 3D systems. Using this approximation we obtain Eq. (5) of the main text:

$$V_{2\text{D}}(\mathbf{r}_{\parallel}) = -E_{\text{Ha}} \frac{a_0 d}{2} \epsilon_{\text{ion}} q_c^2 \phi(q_c r), \quad (\text{S33})$$

where the function ϕ is defined as:

$$\phi(s) = \int_0^{\infty} \frac{x J_0(x) dx}{(s + x)^2}. \quad (\text{S34})$$

To obtain Eq. (6) of the main text we need to carry out the integration in the last expression. We recast this expression as follows:

$$\phi(s) = \left[1 + s \frac{d}{ds} \right] \int_0^{\infty} \frac{J_0(x) dx}{x + s}. \quad (\text{S35})$$

The last integral is equal to $\pi[H_0(s) - Y_0(s)]/2$, where H_0 is the Struve function and Y_0 is the Bessel function of the second kind. After carrying out the derivative in the last equation, we find the Struve and Bessel functions H_1 and Y_1 , leading to Eq. (6) of the main text:

$$\phi(s) = s + \frac{\pi}{2} [H_0(s) - Y_0(s)] - \frac{\pi}{2} s [H_1(s) - Y_1(s)]. \quad (\text{S36})$$

Supplemental Note 5: Derivation of Eq. (7) of the main text

In this Note we derive Eq. (7) of the main text, which gives the formation energy of the polaron corresponding to the variational ansatz:

$$\phi(\mathbf{r}_{\parallel}) = \sqrt{\frac{2}{\pi r_p^2}} \exp(-r/r_p). \quad (\text{S37})$$

For convenience we reproduce below the formation energy as obtained by combining Eqs. (S15), (S25), (S26), (S28), and (S29):

$$E = \frac{\hbar^2}{2m^*} \int d\mathbf{r}_{\parallel} |\nabla \phi(\mathbf{r}_{\parallel})|^2 - \frac{e^2 \epsilon_{\text{ion}} q_c^2 d}{16\pi \epsilon_0} \frac{1}{2\pi} \int_{\text{BZ}_{\parallel}} d\mathbf{q}_{\parallel} \frac{1}{(q_c + q)^2} \left| \int d\mathbf{r}_{\parallel} e^{i\mathbf{q}\cdot\mathbf{r}_{\parallel}} |\phi(\mathbf{r}_{\parallel})|^2 \right|^2. \quad (\text{S38})$$

Replacing the ansatz of Eq. (S37) in the first term of Eq. (S38) gives:

$$\frac{\hbar^2}{2m^*} \int d\mathbf{r}_{\parallel} |\nabla \phi^*(\mathbf{r}_{\parallel})|^2 = \frac{\hbar^2}{2m^*} \frac{2}{\pi r_p^4} \int d\mathbf{r}_{\parallel} e^{-2r/r_p} = \frac{\hbar^2}{2m^* r_p^2}. \quad (\text{S39})$$

This is the kinetic term in Eq. (7) of the main text. For the second term of the right-hand side of Eq. (S38), we first evaluate the Fourier transform of $|\phi(\mathbf{r}_{\parallel})|^2$:

$$\int d\mathbf{r}_{\parallel} e^{i\mathbf{q}\cdot\mathbf{r}_{\parallel}} |\phi(\mathbf{r}_{\parallel})|^2 = \frac{2}{\pi r_p^2} \int_0^{\infty} dr r e^{-2r/r_p} \int_0^{2\pi} d\theta e^{iqr \cos \theta}. \quad (\text{S40})$$

As in Eq. (S31), the last integral is $2\pi J_0(qr)$, therefore we have:

$$\int d\mathbf{r}_{\parallel} e^{i\mathbf{q}\cdot\mathbf{r}_{\parallel}} |\phi(\mathbf{r}_{\parallel})|^2 = s^2 \int_0^{\infty} dx x e^{-sx} J_0(x) = -s^2 \frac{d}{ds} \int_0^{\infty} dx e^{-sx} J_0(x), \quad s = \frac{2}{qr_p}. \quad (\text{S41})$$

The integral on the right is the Laplace transform of the Bessel function, $(1+s^2)^{-1/2}$, therefore we can write:

$$\int d\mathbf{r}_{\parallel} e^{i\mathbf{q}\cdot\mathbf{r}_{\parallel}} |\phi(\mathbf{r}_{\parallel})|^2 = 8(4+q^2 r_p^2)^{-3/2}. \quad (\text{S42})$$

Using this result in the second term of Eq. (S38) we obtain:

$$-\frac{e^2 \epsilon_{\text{ion}} q_c^2 d}{16\pi \epsilon_0} \frac{1}{2\pi} \int_{\text{BZ}_{\parallel}} d\mathbf{q}_{\parallel} \frac{1}{(q_c + q)^2} \left| \int d\mathbf{r}_{\parallel} e^{i\mathbf{q}\cdot\mathbf{r}_{\parallel}} |\phi(\mathbf{r}_{\parallel})|^2 \right|^2 = -\frac{e^2 \epsilon_{\text{ion}} q_c^2 d}{16\pi \epsilon_0} 64 \int_0^{q_{\text{BZ}_{\parallel}} r_p} dx \frac{x}{(q_c r_p + x)^2 (4+x^2)^3}. \quad (\text{S43})$$

As for Eq. (S32), we can extend the integration bound to infinity without making a significant error. Putting Eqs. (S39) and (S43) together, we find Eq. (7) of the main text:

$$E = \frac{\hbar^2}{2m^* r_p^2} - \frac{\epsilon_{\text{ion}}}{4} \frac{e^2 d}{4\pi \epsilon_0 r_p^2} f(q_c r_p), \quad (\text{S44})$$

where the function f is given by:

$$f(s) = 64 s^2 \int_0^{\infty} dx \frac{x}{(s+x)^2 (4+x^2)^3}. \quad (\text{S45})$$

Integration with Mathematica gives the following explicit expression for f :

$$f(s) = \frac{s^2}{(s^2+4)^4} [s^6 - \pi s^5 + 28s^4 - 40\pi s^3 - 16(1+20 \log 2)s^2 + 240\pi s + 64(4 \log 2 - 7) + 64(5s^2 - 4) \log s]. \quad (\text{S46})$$

A plot of this function is shown in Fig. S8.

Supplemental Note 6: Weak coupling expansion

In this Note we derive the weak coupling expansion for the polaron formation energy E and radius r_p in terms of the descriptors β and γ defined in the main text:

$$\beta = \epsilon_{\text{ion}} \frac{m^* d}{m_0 a_0}, \quad (\text{S47})$$

$$\gamma = \frac{(q_c a_0)^2}{m^*/m_0}, \quad q_c = \frac{1}{d} \frac{4\epsilon_{\infty}}{2\epsilon_{\infty}^2 - 1}. \quad (\text{S48})$$

Using Eqs. (S47)-(S48), Eq. (S44) can be rewritten as:

$$\frac{E}{E_{\text{Ha}}} = \frac{\gamma}{4} \frac{2 - \beta f(s)}{s^2}, \quad s = q_c r_p, \quad (\text{S49})$$

with f given by Eq. (S46). The polaron formation energy E is found by minimizing this expression with respect to the scaled polaron radius $s = q_c r_p$. The location of this minimum only depends on the parameter β , therefore the polaron radius r_p depends on β and q_c . Similarly, the value of the formation energy at the minimum depends only on β and γ .

The weak coupling case corresponds to the limit of β approaching 2 from above. In this limit, the polaron radius tends to infinity, therefore we can replace the function f in Eq. (S46) by its asymptotic expansion at large s :

$$f(s) = 1 - \frac{\pi}{s}, \quad s \gg 1. \quad (\text{S50})$$

A plot of this approximation is shown in Fig. S8. Using this expression inside Eq. (S49), and retaining only the leading-order terms in $\beta - 2$, we obtain the polaron radius and energy in the weak-coupling limit:

$$r_p = \frac{1}{q_c} \frac{3\pi}{\beta - 2}, \quad (\text{S51})$$

$$\frac{E}{E_{\text{Ha}}} = -\frac{1}{108 \pi^2} \gamma (\beta - 2)^3. \quad (\text{S52})$$

Equation (S52) yields a formation energy that is within 10% of the value obtained by direct numerical minimization of Eq. (S49) for $\beta < 2.5$.

Supplemental Note S7: Polarons in monolayer ZrS₂, fluorographene, and monolayer BeO

In this Note we report additional calculations of polarons in 2D crystals. We use the *ab initio* polaron equations reported as Eqs. (1)-(2) of the main text, we perform validation tests via self-interaction-corrected DFT (SIC-DFT) and hybrid functionals, and we compare with the analytical model in Eq. (7) of the main text. We consider the following systems:

1. Electron and hole polarons in monolayer ZrS₂;
2. Electron and hole polarons in fluorographene (CF);
3. Hole polaron in monolayer BeO.

1. Electron and hole polarons in monolayer ZrS₂

Calculations using the ab initio polaron equations

Our calculations indicate that monolayer ZrS₂ hosts large electron and hole polarons. The electron polaron is comprised primarily of Zr-4d states as shown by the wavefunction plot in Fig. S9(a). The wavefunction is spatially anisotropic, and we find three degenerate polarons which are related by 60° rotations. Each polaron is formed by Bloch states belonging to pairs of M points that are time-reversal partners, as well as the conduction band minimum at Γ , as shown in Fig. S9(b) and (c). The contribution of vibrational modes to the polaron formation energy are shown in Fig. S9(d), and the corresponding density of states is in Fig. S9(e). The formation energy of the electron polaron in the dilute limit is 189 meV.

Figure S10 shows the corresponding results for the hole polaron in monolayer ZrS₂. In this case, the hole polaron draws weight primarily from the top of the valence band at Γ , which has S-3p character. The formation energy of the hole polaron in the dilute limit is 110 meV.

Calculations using self-interaction corrected DFT

To validate our results for ZrS₂ obtained from the *ab initio* polaron equations, we perform explicit self-interaction-corrected (SIC) DFT calculations using the method of Ref. 20. We consider a supercell of 7×7×1 unit cells (147 atoms). This calculation does not indicate any stable electron polaron, in agreement with the fact that polaron formation is only observed with the *ab initio* polaron equations [Fig. S2(a)] for supercells of at least 10×10×1 unit cells (300 atoms). Therefore, both the *ab initio* polaron equations and SIC-DFT indicate that there are no small electron polarons in ZrS₂.

Calculations using the 2D model

The model of Eq. (7) yields a formation energy of 110 meV for the electron polaron. In this estimate we employed the dielectric constants reported in Supplemental Table S1. In comparison, the *ab initio* polaron equations yield a formation energy of 189 meV, of which 64% results from LO phonons [see Fig. S9(e)]. Therefore the formation energy arising only from Fröhlich interactions is 121 meV, in good agreement with the 2D model.

The model of Eq. (7) also predicts a formation energy of 104 meV for the hole polaron. In comparison, the *ab initio* polaron equations yield a formation energy of 110 meV, of which 94% results from LO phonons [see Fig. S10(d)]. Therefore the contribution of Fröhlich interactions to the formation energy is of 103 meV, which is also in good agreement with the model.

We note that the formation energy is rather sensitive to the values of the dielectric constants. For example, by using the values reported in Ref. 72 ($\epsilon_\infty = 9.9$, $\epsilon_0 = 37.2$), instead of those reported in Supplemental Table S1 ($\epsilon_\infty = 12.2$, $\epsilon_0 = 29.6$), we obtain formation energies of 349 meV and 313 meV for the electron and hole polaron, respectively, as shown in Table S3. This is because the formation energy is rather sensitive to ϵ_{ion} via the descriptor β , see Eq. (S52). Therefore care must be used when estimating polaron formation energies in 2D materials using dielectric constants from bulk 3D compounds.

2. Electron and hole polarons in fluorographene

Calculations using the ab initio polaron equations

Figure S3(a) and (b) show the formation energy of electron and hole polaron in fluorinated graphene (CF) as a function of supercell size. In the case of the electron polaron, the formation energy tends to zero for infinitely large supercells, indicating that fluorographene does not admit localized electron polarons. In the case of holes, we find a weakly-coupled polaron, with a very small formation energy of 1.4 meV in the dilute limit. This polaron draws weight from the $p\sigma$ states at the top of the valence band [Fig. S11(a)], and is primarily driven by the E_u LO modes around 40 meV [Fig. S11(b)]. This very large polaron extends over more than $110 \times 110 \times 1$ unit cells.

Calculations using self-interaction corrected DFT

To validate our results for fluorographene obtained from the *ab initio* polaron equations, we perform explicit supercell calculations of the electron polaron using SIC-DFT. Fig. S3 shows that the formation energy obtained from SIC-DFT tracks closely the results of Eqs. (1)-(2) for large supercell sizes, and also tends to a vanishing formation energy in the dilute limit. The deviation between the two results at small supercell sizes, which can be seen in Fig. S3 for $3 \times 3 \times 1$ and $4 \times 4 \times 1$ supercells, is ascribed to the fact that the SIC-DFT calculations is performed using the CP code of Quantum ESPRESSO (modified to include SIC). Since this code uses Γ -point sampling, its calculations converge more slowly with supercell size than Eqs. (1)-(2). Nevertheless, the two approaches yield practically indistinguishable results for supercells larger than $7 \times 7 \times 1$ unit cells.

Calculations using the 2D model

In the case of the electron polaron, the materials parameters of CF (see Supplemental Table S3) yield a value of the 2D coupling strength $\beta = 1.77$, which is below the critical strength ($\beta = 2$) required for polaron formation. Accordingly, Eq. (7) of the main text predicts that no polaron will form. This result is in agreement with the calculations using the *ab initio* polaron equations and using SIC-DFT described above.

In the case of the hole polaron, the hole mass of fluorographene is heavier than the electron mass ($1.13 m_e$ vs. $0.48 m_e$). As a result, the coupling strength for holes exceeds the critical value, $\beta = 4.16$, and a polaron can form. Equation (7) yields a formation energy of 0.6 meV. Fig. S11(c) shows that the LO mode at 40 meV contributes 88% of the formation energy; therefore, when considering only the Fröhlich interaction, the polaron equations yield a formation energy of 1.2 meV, in good agreement with the 2D model. In practice, this hole polaron is so weakly coupled that it is unlikely to be observable in experiments.

3. Hole polaron in monolayer BeO

Calculations using the ab initio polaron equations

In the case of BeO monolayer, the solution of the *ab initio* polaron equations yields a small hole polaron. Fig S12(a) shows that the polaron is primarily localized on a single O site, with minor contributions from second-nearest-neighbor O atoms. This small polaron has a large formation energy of 596 meV, which is a sizeable fraction of the DFT band gap of this compound (5.3 eV). Analysis of the Fourier amplitudes of the hole wavefunction and of the atomic displacements [Fig. S12(c)] reveals that this particle is a small Fröhlich polaron, with electronic contributions from the valence band top at K (O-2p states) and vibrational contributions from the high-frequency LO modes and low-frequency piezoacoustic modes at long wavelength [Fig S12(d)].

Calculations using the HSE hybrid functional

To validate our results for monolayer BeO based on the *ab initio* polaron equations, we perform explicit supercell calculations of the hole polaron using the HSE functional [101]. This calculation is feasible because the small polaron fits in a 5×5 supercell (50 atoms). We find that the polaron only forms when the exchange fraction α in the functional exceeds the critical value $\alpha_c = 0.29$, in line with our analysis in Supplemental Note 1. For $\alpha > 0.29$, we obtain a

small hole polaron as shown in Fig. S12(b). A comparison between Figs. S12(a) and (b) shows that the wavefunction produced by the *ab initio* polaron equations, and that obtained from HSE, are practically indistinguishable. This comparison further validates the present approach. For $\alpha > 0.29$, the HSE energy of the polaron increases monotonically with α ; this is an artifact of the HSE functional as discussed in Supplemental Note 1, therefore a comparison of the energies between HSE calculations and Eqs. (1)-(2) is not meaningful.

Calculations using the 2D model

In the case of the hole polaron in BeO, the model of Eq. (7) yields a formation energy of 266 meV. In this estimate we employed the dielectric constants reported in Supplemental Table S1. Our explicit calculations using Eqs. (1)-(2) indicate a small hole polaron with formation energy of 596 meV, and the contribution from the LO modes is of 61%. Therefore the formation energy resulting from the Fröhlich interaction is 364 meV, which is 37% larger than the model hence in line with our prediction.

As for ZrS₂, the formation energy is sensitive to the values of the dielectric constants. For example, by using the dielectric constants reported in Supplemental Table S3 instead of those in Supplemental Table S1, we obtain a formation energy of 218 meV, as shown in Supplemental Table S3.

Material	d (Å)	ϵ_∞	ϵ_0	m_h^*	m_e^*
monolayer h-BN	2.65	5.70	7.92	0.65	0.94
monolayer ZrS ₂	5.22	12.25	29.61	0.29	0.30
fluorographene	4.84	3.44	3.87	1.11	0.48
monolayer BeO	3.11	2.74	4.38	3.34	0.83

TABLE S1. Effective thickness (d), dielectric constants (ϵ_∞ , ϵ_0), and effective masses (m_h^* , m_e^*) of the monolayer compounds considered in this work. The dielectric constants are defined unambiguously by requiring that the screening in the layer be isotropic, following Ref. 48. To this aim, we compute the dielectric permittivities of each supercell, and extract the effective thickness and layer permittivities using Eqs. (64) and (65) of Ref. 21.

	3D	2D
Matrix element	$ g(q) ^2 = E_{\text{Ha}} \hbar \omega a_0 \frac{2\pi}{\Omega \kappa} \frac{1}{q^2}$	$ g(q) ^2 = E_{\text{Ha}} \hbar \omega a_0 \frac{\pi \epsilon_{\text{ion}} (q_c d)^2}{2Ad} \frac{1}{(q_c + q)^2}$ $q_c d = 4\epsilon_{\infty} / (2\epsilon_{\infty}^2 - 1)$
Effective potential	$V_{3\text{D}}(r) = -\frac{E_{\text{Ha}} a_0}{\kappa} \frac{1}{r}$	$V_{2\text{D}}(r) = -\frac{1}{2} E_{\text{Ha}} a_0 d q_c^2 \epsilon_{\text{ion}} \phi(q_c r)$ $\phi(s) = s + \frac{\pi}{2} [H_0(s) - Y_0(s)] - \frac{\pi}{2} s [H_1(s) - Y_1(s)]$
Wavefunction ansatz	$\psi = (\pi r_p^3)^{-1/2} \exp(- \mathbf{r} /r_p)$	$\psi = (2/\pi r_p^2)^{1/2} \exp(- \mathbf{r} /r_p)$
Formation energy	$E = \frac{\hbar^2}{2m^* r_p^2} - \frac{5}{16} \frac{1}{\kappa} \frac{e^2}{4\pi\epsilon_0 r_p}$	$E = \frac{\hbar^2}{2m^* r_p^2} - \frac{\epsilon_{\text{ion}}}{4} \frac{e^2 d}{4\pi\epsilon_0 r_p^2} f(q_c r_p)$ $f(x) = x^2 [x^6 - \pi x^5 + 28x^4 - 40\pi x^3 - 16(1 + 20 \log 2)x^2 + 240\pi x + 64(4 \log 2 - 7) + 64(5x^2 - 4) \log x] / (x^2 + 4)^4$

TABLE S2. Comparison between the matrix elements, effective potentials, wavefunction ansatz, and formation energies in the Landau-Pekar model in 3D [20, 52] and the present 2D model. H_0 and H_1 are Struve functions, and Y_0 and Y_1 are Bessel functions of the second kind. In both cases, the formation energy is obtained by replacing the variational ansatz inside the functional $E = \frac{\hbar^2}{2m^*} \int d\mathbf{r} |\nabla\psi|^2 + \frac{1}{2} \int d\mathbf{r} d\mathbf{r}' |\psi(\mathbf{r})|^2 V(\mathbf{r} - \mathbf{r}') |\psi(\mathbf{r}')|^2$, where the integral is in three dimensions or two dimensions, respectively, and $V(r)$ is replaced by $V_{3\text{D}}$ or $V_{2\text{D}}$ given in the table.

	Material	m^* (m_e)	ϵ_∞	ϵ_0	d (Å)	q_c (Å ⁻¹)	β	$\gamma \cdot 10^3$	E (meV)	r_p (Å)
Holes	h-BN	0.65	5.0	6.9	3.12	0.131	7.28	7.37	-10.8	15.8
	MoS ₂	0.57	15.8	15.9	6.09	0.021	0.66	0.21	-	-
	MoSe ₂	0.65	17.2	17.7	6.48	0.018	3.98	0.14	0.0	275.4
	MoTe ₂	0.72	20.1	21.9	7.08	0.014	17.34	0.08	-1.1	63.1
	WS ₂	0.42	14.4	14.4	6.10	0.023	0.00	0.35	-	-
	WSe ₂	0.45	15.6	15.9	6.47	0.020	1.65	0.25	-	-
	HfS ₂	0.44	10.4	48.9	5.72	0.034	183.11	0.73	-646.0	5.3
	HfSe ₂	0.23	13.9	71.2	6.11	0.024	152.17	0.68	-458.0	8.4
	ZrS ₂	0.26	9.9	37.2	5.71	0.036	76.59	1.36	-313.1	8.6
	InSe	2.60	8.8	11.2	8.00	0.029	94.34	0.09	-28.3	9.3
	CF	1.13	3.13	3.48	5.57	0.121	4.16	3.62	-0.6	37.7
	BeO	3.52	2.74	4.18	3.03	0.258	29.02	5.30	-217.9	2.3
	AlN	1.49	4.46	7.31	2.09	0.220	16.77	9.10	-119.8	4.2
	GaN	1.35	6.17	9.05	2.45	0.134	18.00	3.73	-57.4	6.4
Electrons	h-BN	0.83	5.0	6.9	3.12	0.131	9.30	5.77	-17.5	12.1
	MoS ₂	0.45	15.8	15.9	6.09	0.021	0.52	0.27	-	-
	MoSe ₂	0.54	17.2	17.7	6.48	0.018	3.31	0.17	0.0	408.3
	MoTe ₂	0.56	20.1	21.9	7.08	0.014	13.49	0.10	-0.8	78.5
	WS ₂	0.31	14.4	14.4	6.10	0.023	0.00	0.47	-	-
	WSe ₂	0.34	15.6	15.9	6.47	0.020	1.25	0.32	-	-
	HfS ₂	0.24	10.4	48.9	5.72	0.034	99.88	1.33	-469.0	7.6
	HfSe ₂	0.18	13.9	71.2	6.11	0.024	119.09	0.87	-402.4	9.8
	ZrS ₂	0.31	9.9	37.2	5.71	0.036	91.32	1.14	-349.0	7.7
	InSe	0.10	8.8	11.2	8.00	0.029	3.63	2.29	-0.2	208.1
	CF	0.48	3.13	3.48	5.57	0.121	1.77	8.53	-	-
	BeO	0.83	2.74	4.18	3.03	0.258	6.84	22.47	-26.9	8.6
	AlN	0.51	4.46	7.31	2.09	0.220	5.74	26.60	-17.2	12.6
	GaN	0.24	6.17	9.05	2.45	0.134	3.20	20.97	-0.7	59.4

TABLE S3. Polaron formation energy E and radius r_p of 2D materials, as estimated using Eq. (7) of the main text. The materials parameters β , γ , and q_c have been obtained from the definitions given in the main text, using calculated effective masses and dielectric constants from the literature. The hole effective masses correspond to calculations for the monolayers, and are taken from the following references: h-BN: Ref. 21; MoS₂, MoSe₂, MoTe₂, WS₂, WSe₂: Ref. 48; HfS₂: Ref. 66; HfSe₂: Ref. 102; ZrS₂: Ref. 67; InSe: Ref. 68 (β phase); CF: Ref. 103; BeO: Ref. 104; AlN: Ref. 105; GaN: Ref. 106. The electron effective masses correspond to calculations for the monolayers, and are taken from the following references: h-BN: Ref. 69; MoS₂, MoSe₂, MoTe₂, WS₂, WSe₂: Ref. 48; HfS₂, HfSe₂, ZrS₂: Ref. 70; InSe: Ref. 68. (β phase); CF: Ref. 103; BeO: Ref. 107; AlN: Ref. 105; GaN: Ref. 106. In the case of HfS₂, HfSe₂, ZrS₂ the masses are anisotropic and we use the lowest mass reported. The dielectric constants are calculations for bulk crystals, in the in-plane direction, and are taken from Ref. 71 for all systems except for ZrS₂, which is from Ref. 72, InSe, which is from Ref. 73 (γ phase), and BeO, AlN, GaN. For these latter compounds, the bulk crystals take the wurtzite structure, therefore the bulk dielectric constants are not available; in these cases we calculated the bulk dielectric constants for the metastable hexagonal phases with AA' stacking. In all cases, the thickness d is set to the calculated interlayer distance, taken from Refs. 68 and 71. Dashes “-” indicate that localized polaron wavefunctions do not exist. We note that the formation energies E in the penultimate column are sensitive to the precise values of the static and high-frequency dielectric constants. For example, by using the values in Supplemental Table S1, which we calculated using the procedure of Ref. 48, instead of the literature values reported in this table, we obtain formation energies of 110 meV and 104 meV for the electron and hole polarons in monolayer ZrS₂, and a formation energy of 266 meV for the hole polaron in BeO (see Supplemental Note S7). This sensitivity must be taken into account when performing high-throughput screenings of the polaronic properties of 2D materials.

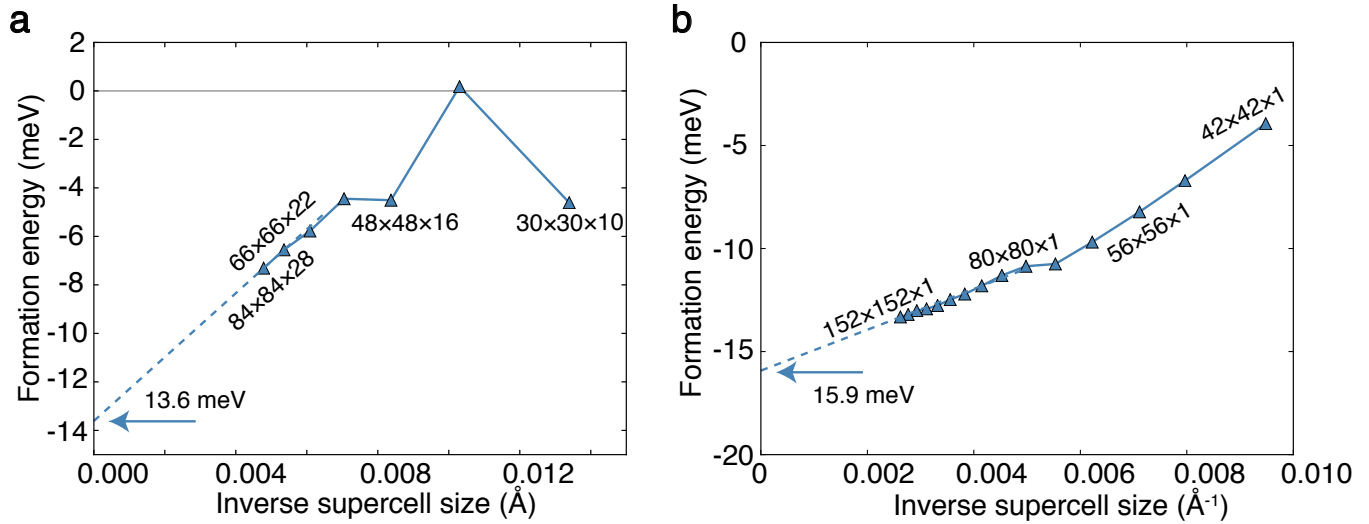


FIG. S1. Formation energy of hole polaron in h-BN as a function of inverse supercell size, for (a) bulk h-BN and (b) monolayer h-BN. The numbers next to some of the data points indicate the supercell dimension as a multiple of the crystalline unit cell. The dashed line is the linear extrapolation based on the last 3 data points, following the procedure outlined in Ref. 20. The extrapolation to infinite supercell size provides the formation energy of the isolated polaron.

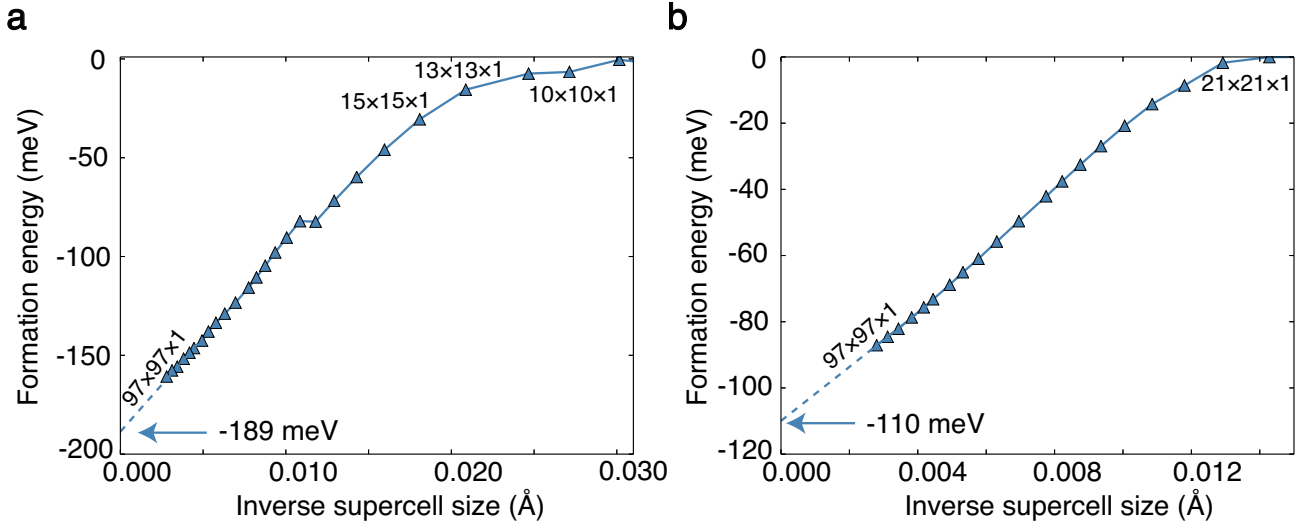


FIG. S2. Formation energy of (a) electron polaron and (b) hole polaron of monolayer ZrS_2 . The numbers next to some of the data points indicate the supercell dimension as a multiple of the crystalline unit cell. The dashed line is the linear extrapolation as in Fig. S1, and the intercept with the vertical axis indicates the formation energy in the dilute limit.

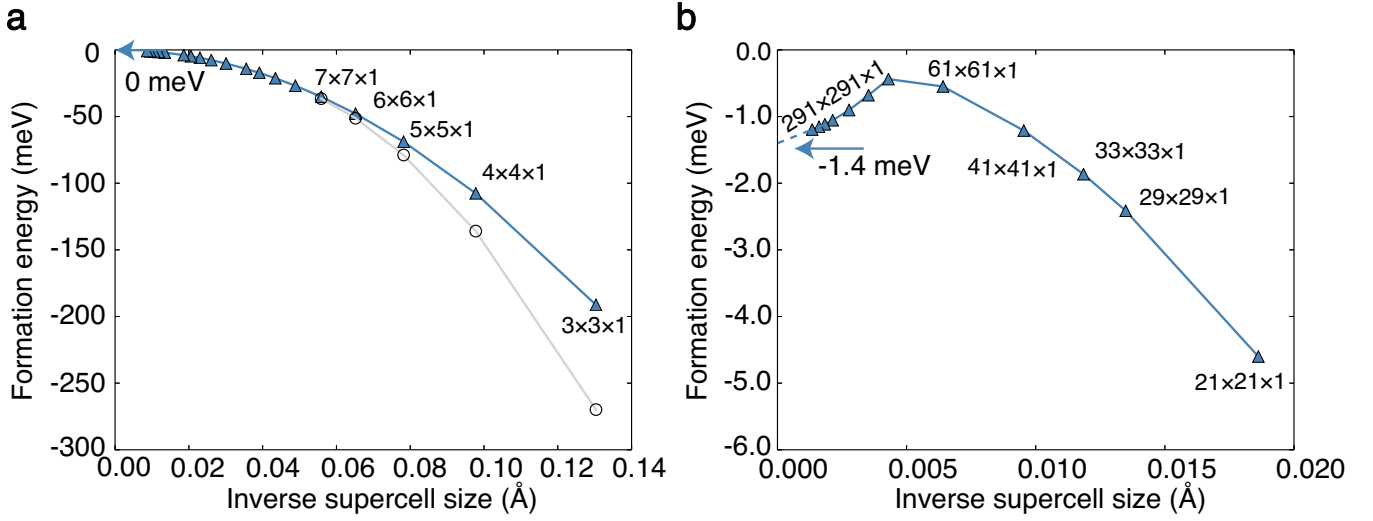


FIG. S3. Formation energy of (a) electron polaron and (b) hole polaron of monolayer fluorographene, as obtained via the *ab initio* polaron equations (filled triangles). The numbers next to some of the data points indicate the supercell dimension as a multiple of the crystalline unit cell. In (a) we also show the formation energy of the electron polaron, as obtained from explicit supercell calculations using SIC-DFT (circles). In (b), the dashed line is the linear extrapolation as in Fig. S1, and the intercept with the vertical axis indicates the formation energy in the dilute limit.

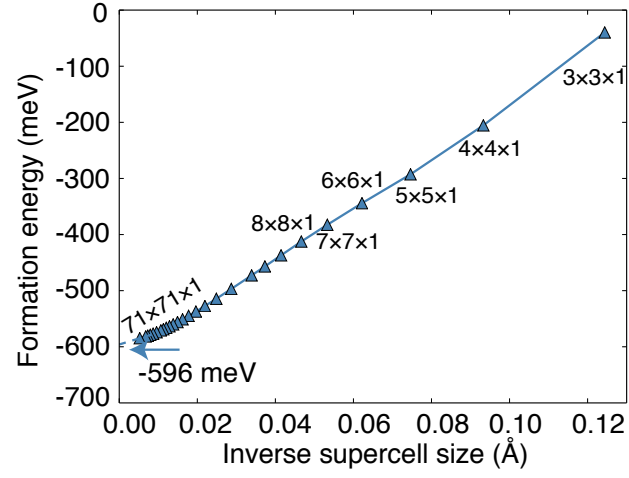


FIG. S4. Formation energy of hole polaron of monolayer BeO. The numbers next to some of the data points indicate the supercell dimension as a multiple of the crystalline unit cell. The dashed line is the linear extrapolation as in Fig. S1, and the intercept with the vertical axis indicates the formation energy in the dilute limit.

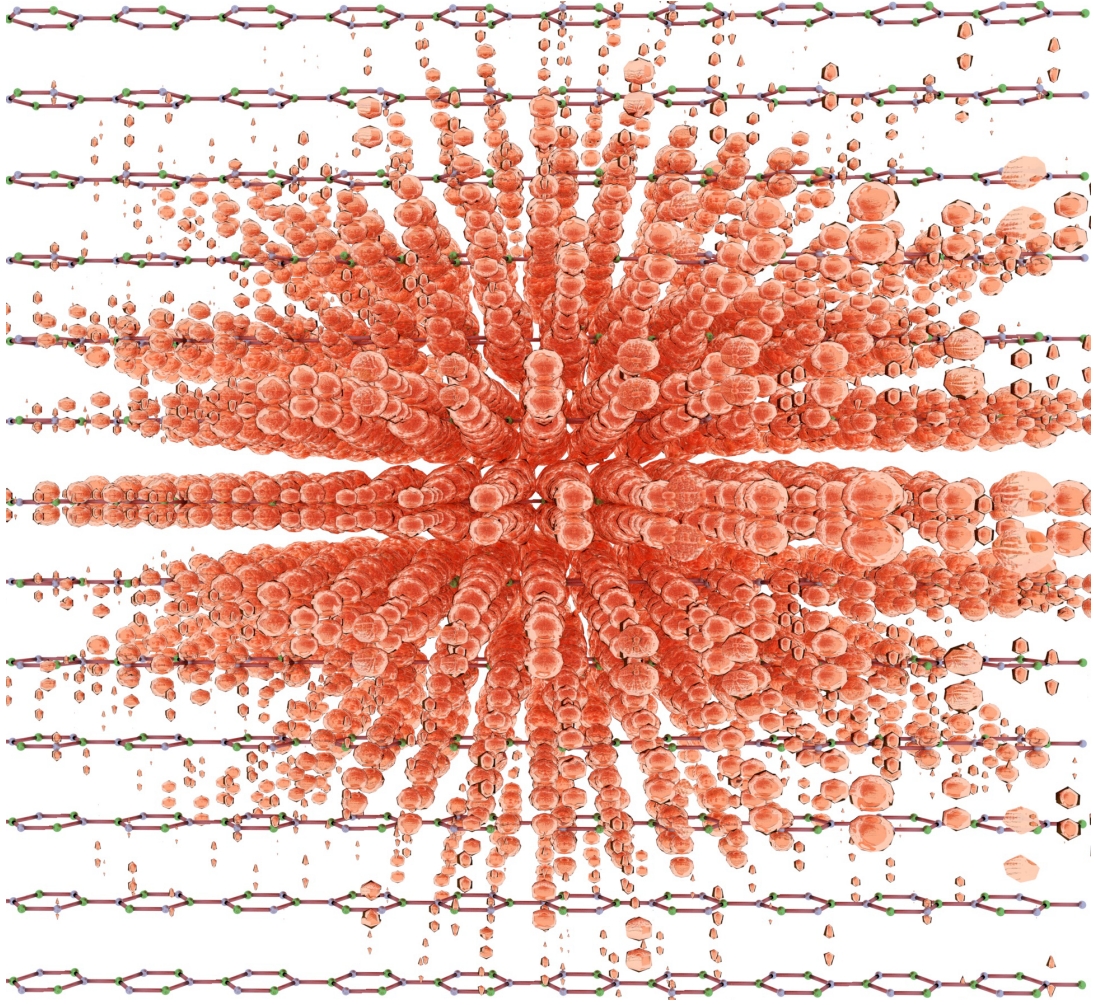


FIG. S5. Enlarged view of the hole polaron in bulk h-BN, shown in Fig. 1(c) of the main text. The plot represents an isosurface of the hole polaron density $|\psi(\mathbf{r})|^2$ for a $24 \times 24 \times 8$ supercell (9216 atoms).

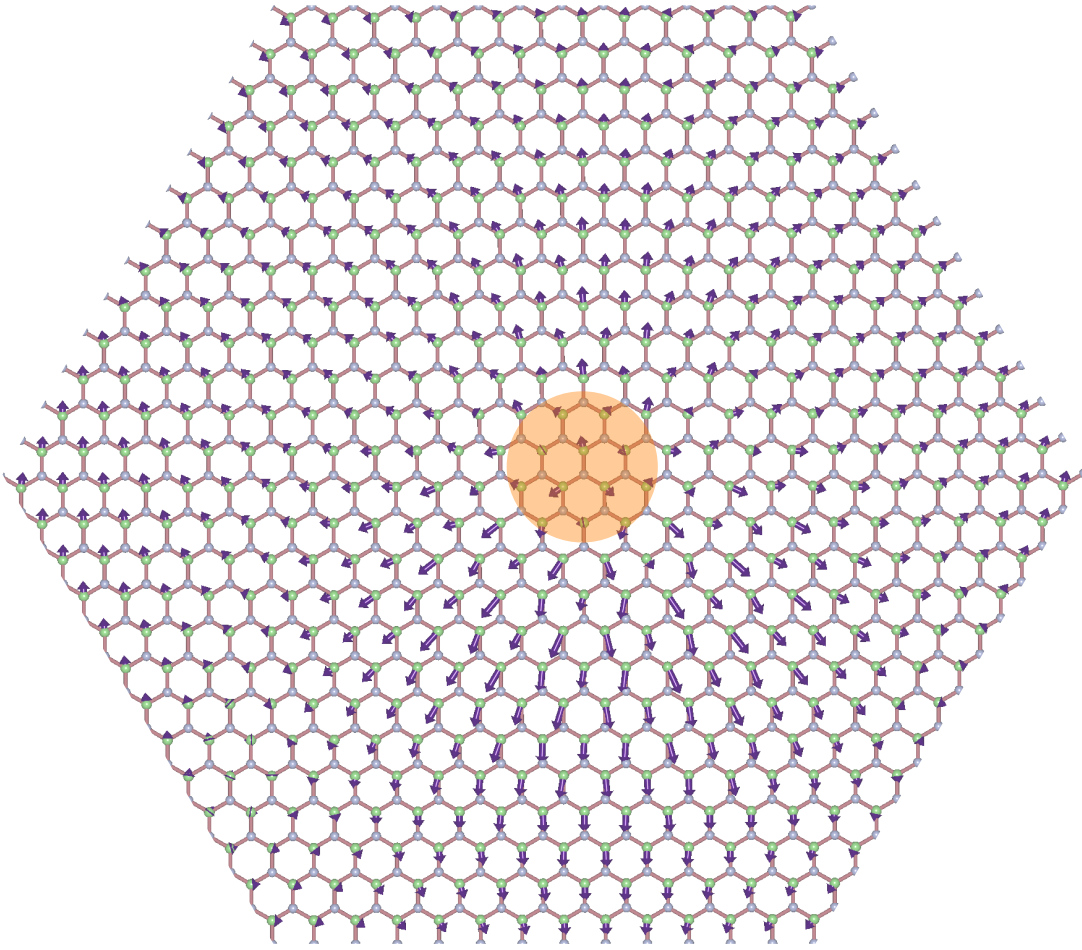


FIG. S6. Atomic displacements of the boron atoms associated with the hole polaron state in monolayer h-BN. This calculation corresponds to a $26 \times 26 \times 1$ supercell. The arrows have been exaggerated ($\times 300$) for ease of visualization. The center of the polaron wavefunction shown in Fig. 2(d) of the main text is labeled by a disk.

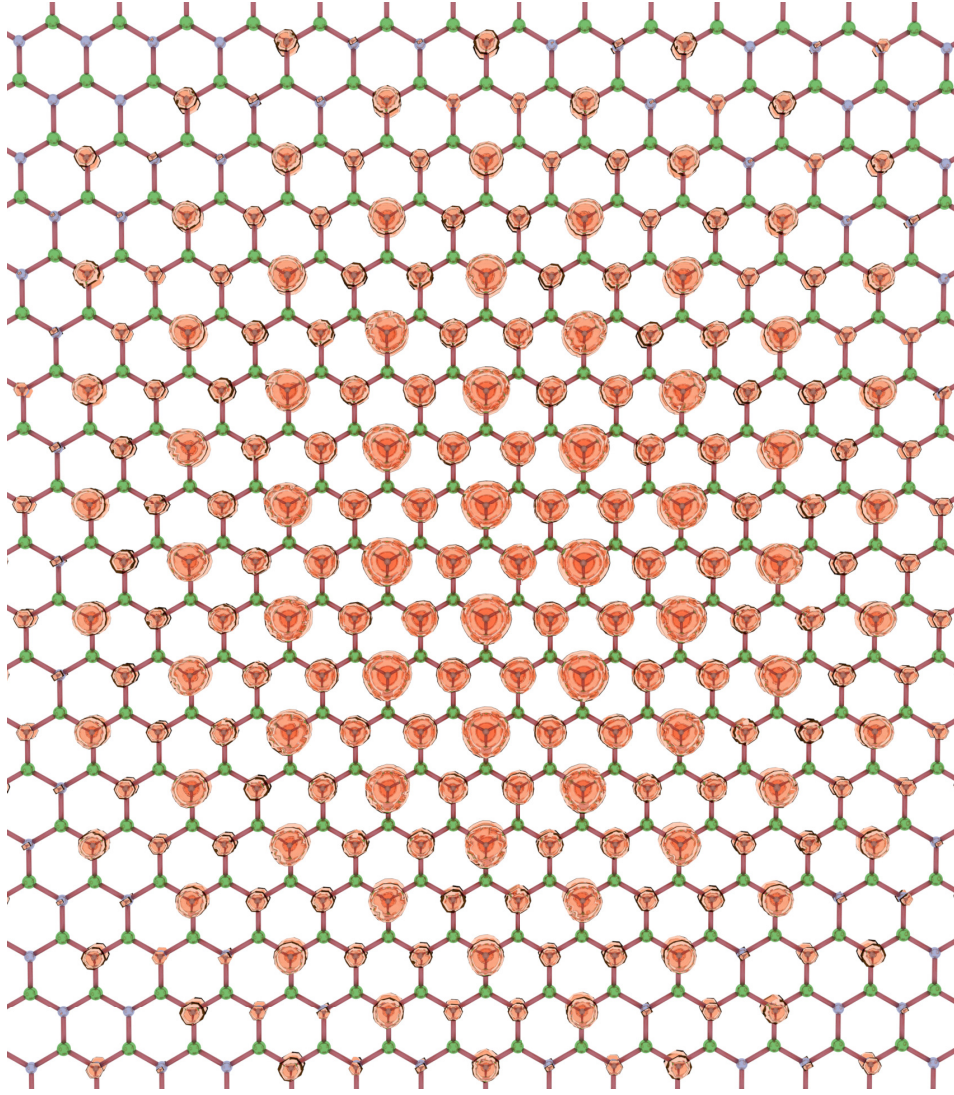


FIG. S7. Enlarged view of the hole polaron in monolayer h-BN, shown in Fig. 2(d) of the main text. The plot represents an isosurface of the hole polaron density $|\psi(\mathbf{r})|^2$ for a $26 \times 26 \times 1$ supercell (676 atoms).

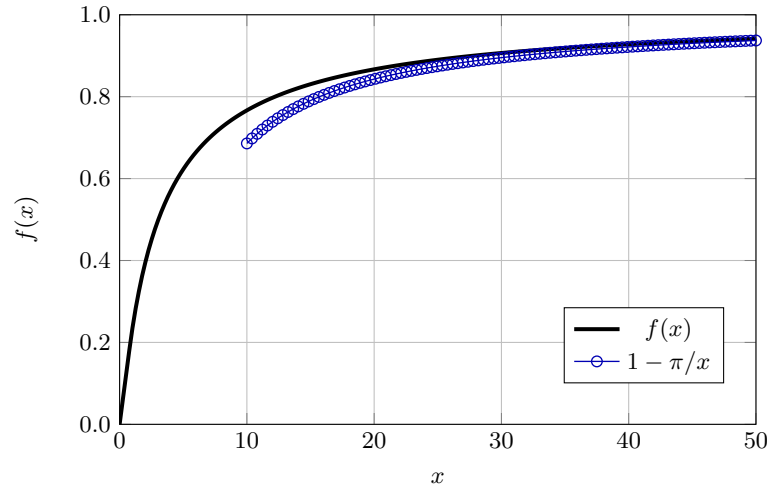


FIG. S8. Plot of the dimensionless function $f(x)$ appearing in the polaron formation energy, Eq. (S49) (black solid line) and its asymptotic expansion $1 - \pi/x$ (blue circles).

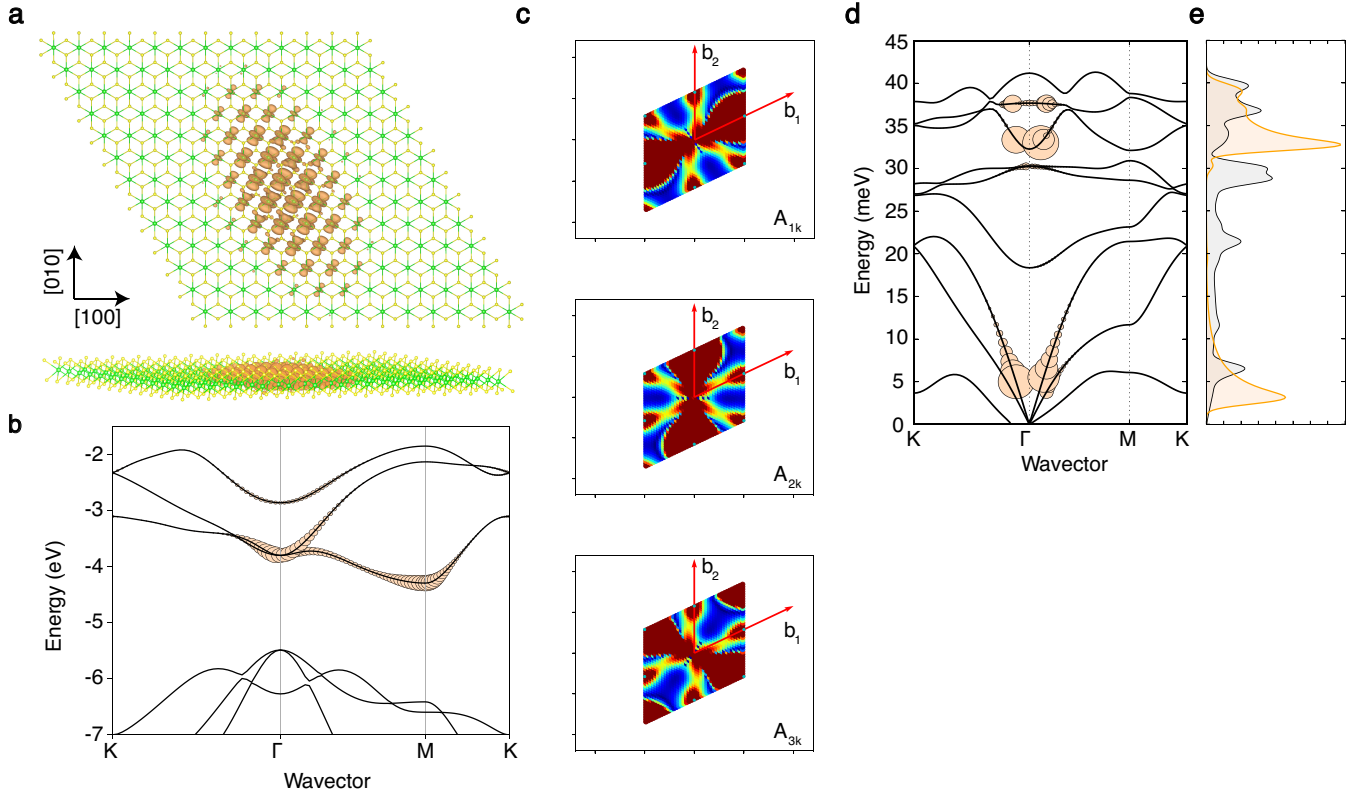


FIG. S9. Electron polaron in monolayer ZrS₂. (a) Isosurface plot of the polaron wavefunction, with side view and top view. (b) Band structure of monolayer ZrS₂, with the Fourier amplitudes $A_{n\mathbf{k}}$ of the polaron superimposed as circles. The radius of the circles is proportional to $|A_{n\mathbf{k}}|^2$. (c) 2D colormap plot of the coefficients $|A_{n\mathbf{k}}|^2$ for the three degenerate polaron states, showing threefold rotation symmetry. (d) Phonon dispersions with the Fourier amplitudes $B_{\mathbf{q}\nu}$ superimposed as circles. (e) Phonon density of states (black) and spectral decomposition of the vibrational contribution to the formation energy (orange).

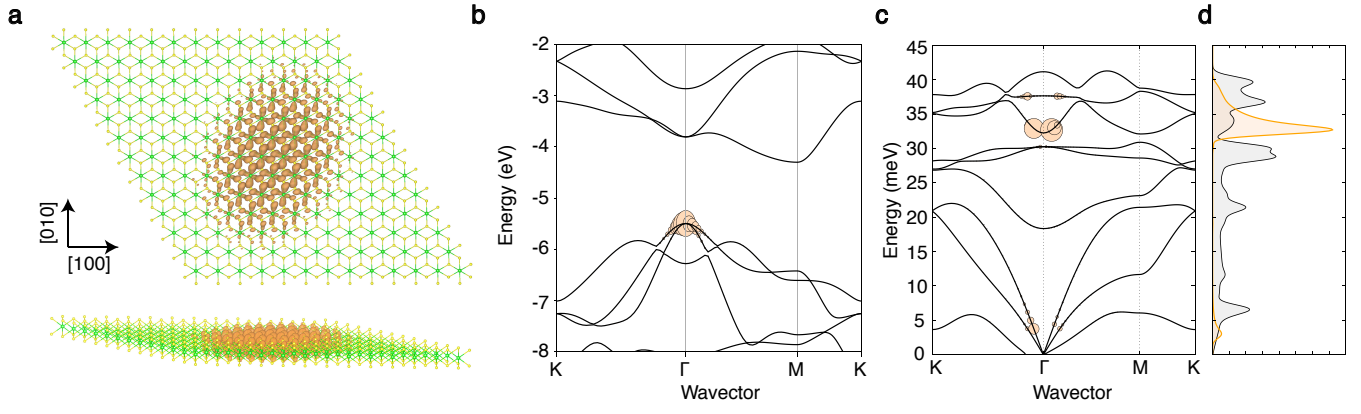


FIG. S10. Hole polaron in monolayer ZrS₂. (a) Isosurface plot of the polaron wavefunction, with side view and top view. (b) Band structure of monolayer ZrS₂, with the Fourier amplitudes $A_{n\mathbf{k}}$ of the polaron superimposed as circles. (c) Phonon dispersions with the Fourier amplitudes $B_{\mathbf{q}\nu}$ superimposed as circles. (d) Phonon density of states (black) and spectral decomposition of the vibrational contribution to the formation energy (orange).

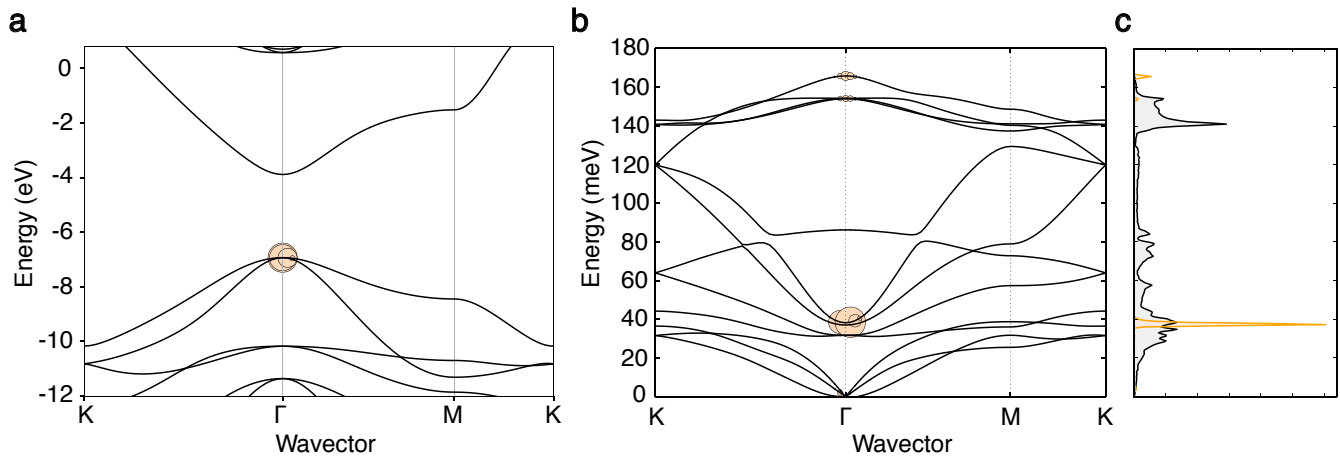


FIG. S11. Hole polaron in fluorographene. (a) Band structure of monolayer CF, with the Fourier amplitudes $A_{n\mathbf{k}}$ of the polaron superimposed as circles. (b) Phonon dispersions of monolayer CF, with the Fourier amplitudes $B_{\mathbf{q}\nu}$ superimposed as circles. (c) Phonon density of states (black) and spectral decomposition of the vibrational contribution to the formation energy (orange).

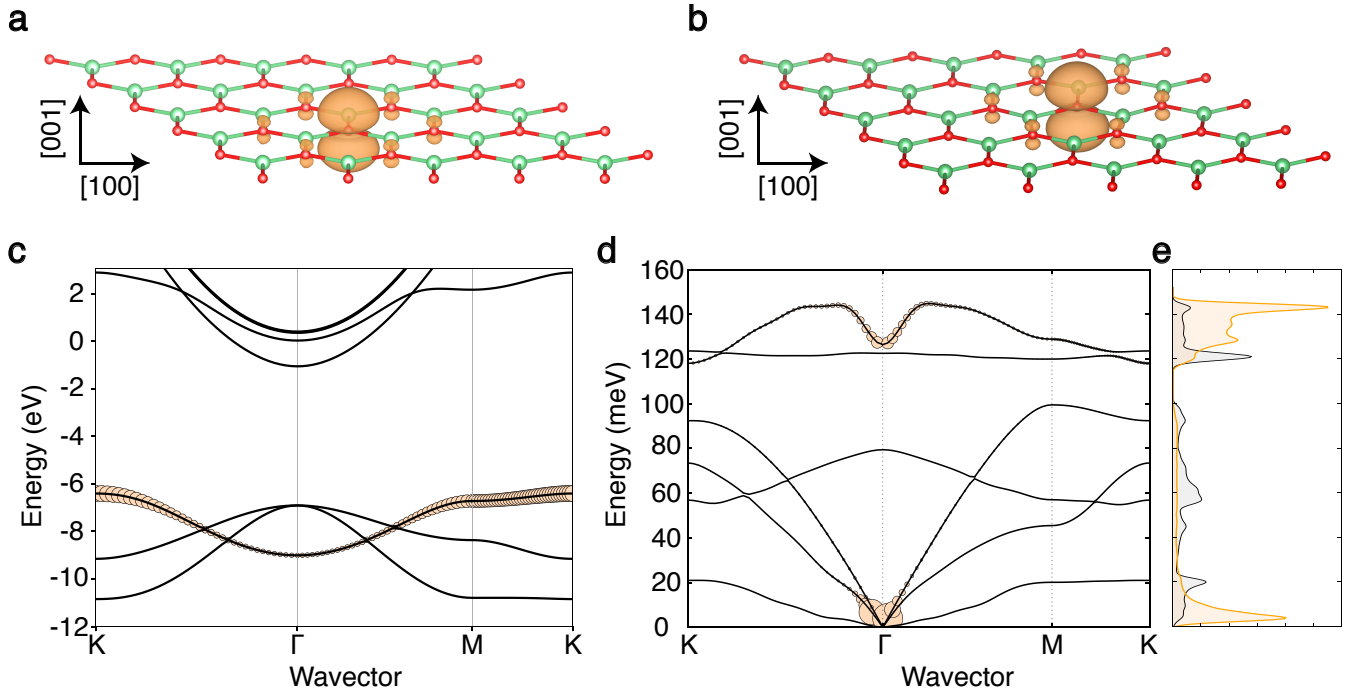


FIG. S12. Hole polaron in monolayer BeO. (a) Polaron wavefunction as obtained from the solution of the *ab initio* polaron equations. (b) Polaron wavefunction as obtained by explicit supercell calculations using the HSE hybrid functional, with $\alpha = 0.37$. (c) Band structure of monolayer BeO, with the Fourier amplitudes $A_{n\mathbf{k}}$ of the polaron superimposed as circles. (d) Phonon dispersions of monolayer BeO, with the Fourier amplitudes $B_{\mathbf{q}\nu}$ superimposed as circles. (e) Phonon density of states (black) and spectral decomposition of the vibrational contribution to the polaron formation energy (orange).

References

- [1] C. Franchini, M. Reticcioli, M. Setvin, and U. Diebold, Polarons in materials, *Nat. Rev. Mater.* **6**, 560 (2021).
- [2] D. Emin, *Polarons* (Cambridge University Press, Cambridge, England, 2012).
- [3] A. S. Alexandrov and J. T. Devreese, *Advances in Polaron Physics*, Springer Series in Solid-State Sciences (Springer, Berlin, Germany, 2012).
- [4] J. M. Riley, F. Caruso, C. Verdi, L. B. Duffy, M. D. Watson, L. Bawden, K. Volckaert, G. van der Laan, T. Hesjedal, M. Hoesch, F. Giustino, and P. D. C. King, Crossover from lattice to plasmonic polarons of a spin-polarised electron gas in ferromagnetic EuO, *Nat. Commun.* **9** (2018).
- [5] Z. Wang, S. McKeown Walker, A. Tamai, Y. Wang, Z. Ristic, F. Y. Bruno, A. de la Torre, S. Riccò, N. C. Plumb, M. Shi, P. Hlawenka, J. Sánchez-Barriga, A. Varykhalov, T. K. Kim, M. Hoesch, P. D. C. King, W. Meevasana, U. Diebold, J. Mesot, B. Moritz, T. P. Devereaux, M. Radovic, and F. Baumberger, Tailoring the nature and strength of electron-phonon interactions in the SrTiO₃(001) 2D electron liquid, *Nat. Mater.* **15**, 835 (2016).
- [6] C. Chen, J. Avila, E. Frantzeskakis, A. Levy, and M. C. Asensio, Observation of a two-dimensional liquid of fröhlich polarons at the bare SrTiO₃ surface, *Nat. Commun.* **6**, 8585 (2015).
- [7] C. Cancellieri, A. S. Mishchenko, U. Aschauer, A. Filippetti, C. Faber, O. S. Barišić, V. A. Rogalev, T. Schmitt, N. Nagaosa, and V. N. Strocov, Polaronic metal state at the LaAlO₃/SrTiO₃ interface, *Nat. Commun.* **7**, 10386 (2016).
- [8] E. Pastor, J.-S. Park, L. Steier, S. Kim, M. Grätzel, J. R. Durrant, A. Walsh, and A. A. Bakulin, In situ observation of picosecond polaron self-localisation in α -Fe₂O₃ photoelectrochemical cells, *Nat. Commun.* **10**, 3962 (2019).
- [9] S. Moser, L. Moreschini, J. Jaćimović, O. S. Barišić, H. Berger, A. Magrez, Y. J. Chang, K. S. Kim, A. Bostwick, E. Rotenberg, L. Forró, and M. Grioni, Tunable polaronic conduction in anatase TiO₂, *Phys. Rev. Lett.* **110**, 196403 (2013).
- [10] E. Baldini, C. A. Belvin, M. Rodriguez-Vega, I. O. Ozel, D. Legut, A. Kozłowski, A. M. Oleś, K. Parlinski, P. Piekarczyk, J. Lorenzana, G. A. Fiete, and N. Gedik, Discovery of the soft electronic modes of the trimeron order in magnetite, *Nat. Phys.* **16**, 541 (2020).
- [11] K. Miyata and X.-Y. Zhu, Ferroelectric large polarons, *Nat. Mater.* **17**, 379 (2018).
- [12] B. Guzelturk, T. Winkler, T. W. J. Van de Goor, M. D. Smith, S. A. Bourelle, S. Feldmann, M. Trigo, S. W. Teitelbaum, H.-G. Steinrück, G. A. de la Pena, R. Alonso-Mori, D. Zhu, T. Sato, H. I. Karunadasa, M. F. Toney, F. Deschler, and A. M. Lindenberg, Visualization of dynamic polaronic strain fields in hybrid lead halide perovskites, *Nat. Mater.* **20**, 618 (2021).
- [13] K. Miyata, D. Meggiolaro, M. T. Trinh, P. P. Joshi, E. Mosconi, S. C. Jones, F. De Angelis, and X.-Y. Zhu, Large polarons in lead halide perovskites, *Sci. Adv.* **3**, e1701217 (2017).
- [14] B. Wu, W. Ning, Q. Xu, M. Manjappa, M. Feng, S. Ye, J. Fu, S. Lie, T. Yin, F. Wang, T. W. Goh, P. C. Harikesh, Y. K. E. Tay, Z. X. Shen, F. Huang, R. Singh, G. Zhou, F. Gao, and T. C. Sum, Strong self-trapping by deformation potential limits photovoltaic performance in bismuth double perovskite, *Sci. Adv.* **7**, eabd3160 (2021).
- [15] K. S. Novoselov, D. Jiang, F. Schedin, T. J. Booth, V. V. Khotkevich, S. V. Morozov, and A. K. Geim, Two-dimensional atomic crystals, *Proc. Natl. Acad. Sci. U. S. A.* **102**, 10451 (2005).
- [16] K. S. Novoselov, A. Mishchenko, A. Carvalho, and A. H. Castro Neto, 2D materials and van der waals heterostructures, *Science* **353**, aac9439 (2016).
- [17] C. Chen, J. Avila, S. Wang, Y. Wang, M. Mucha-Kruczyński, C. Shen, R. Yang, B. Nosarzewski, T. P. Devereaux, G. Zhang, and M. C. Asensio, Emergence of interfacial polarons from electron-phonon coupling in graphene/h-BN van der waals heterostructures, *Nano Lett.* **18**, 1082 (2018).
- [18] M. Kang, S. W. Jung, W. J. Shin, Y. Sohn, S. H. Ryu, T. K. Kim, M. Hoesch, and K. S. Kim, Holstein polaron in a valley-degenerate two-dimensional semiconductor, *Nat. Mater.* **17**, 676 (2018).
- [19] W. H. Sio, C. Verdi, S. Poncé, and F. Giustino, Polarons from first principles, without supercells, *Phys. Rev. Lett.* **122**, 246403 (2019).
- [20] W. H. Sio, C. Verdi, S. Poncé, and F. Giustino, Ab initio theory of polarons: Formalism and applications, *Phys. Rev. B* **99**, 235139 (2019).
- [21] W. H. Sio and F. Giustino, Unified *ab initio* description of fröhlich electron-phonon interactions in two-dimensional and three-dimensional materials, *Phys. Rev. B*, *in press*; arXiv preprint arXiv:2203.00568 (2022).
- [22] F. Giustino, Electron-phonon interactions from first principles, *Rev. Mod. Phys.* **89**, 015003 (2017).
- [23] P. Giannozzi, O. Andreussi, T. Brumme, O. Bunau, M. Buongiorno Nardelli, M. Calandra, R. Car, C. Cavazzoni, D. Ceresoli, M. Cococcioni, N. Colonna, I. Carnimeo, A. Dal Corso, S. de Gironcoli, P. Delugas, R. A. DiStasio, Jr, A. Ferretti, A. Floris, G. Fratesi, G. Fugallo, R. Gebauer, U. Gerstmann, F. Giustino, T. Gorni, J. Jia, M. Kawamura, H.-Y. Ko, A. Kokalj, E. Küçükbenli, M. Lazzeri, M. Marsili, N. Marzari, F. Mauri, N. L. Nguyen, H.-V. Nguyen, A. Otero-de-la Roza, L. Paulatto, S. Poncé, D. Rocca, R. Sabatini, B. Santra, M. Schlipf, A. P. Seitsonen, A. Smogunov, I. Timrov,

- T. Thonhauser, P. Umari, N. Vast, X. Wu, and S. Baroni, Advanced capabilities for materials modelling with quantum ESPRESSO, *J. Phys. Condens. Matter* **29**, 465901 (2017).
- [24] A. A. Mostofi, J. R. Yates, G. Pizzi, Y.-S. Lee, I. Souza, D. Vanderbilt, and N. Marzari, An updated version of wannier90: A tool for obtaining maximally-localised wannier functions, *Comput. Phys. Commun.* **185**, 2309 (2014).
- [25] S. Ponc e, E. R. Margine, C. Verdi, and F. Giustino, EPW: Electron–phonon coupling, transport and superconducting properties using maximally localized Wannier functions, *Comput. Phys. Commun.* **209**, 116 (2016).
- [26] T. Sohler, M. Gibertini, M. Calandra, F. Mauri, and N. Marzari, Breakdown of optical phonons’ splitting in two-dimensional materials, *Nano Lett.* **17**, 3758 (2017).
- [27] D. Wickramaratne, L. Weston, and C. G. Van de Walle, Monolayer to bulk properties of hexagonal boron nitride, *J. Phys. Chem. C* **122**, 25524 (2018).
- [28] B. Arnaud, S. Leb egue, P. Rabiller, and M. Alouani, Huge excitonic effects in layered hexagonal boron nitride, *Phys. Rev. Lett.* **96**, 026402 (2006).
- [29] L. Wirtz, A. Marini, M. Gr uning, C. Attaccalite, G. Kresse, and A. Rubio, Comment on “huge excitonic effects in layered hexagonal boron nitride”, *Phys. Rev. Lett.* **100**, 189701 (2008).
- [30] T. Galvani, F. Paleari, H. P. C. Miranda, A. Molina-S anchez, L. Wirtz, S. Latil, H. Amara, and F. Ducastelle, Excitons in boron nitride single layer, *Phys. Rev. B* **94**, 125303 (2016).
- [31] F. Zhang, C. S. Ong, J. W. Ruan, M. Wu, X. Q. Shi, Z. K. Tang, and S. G. Louie, Intervalley excitonic hybridization, optical selection rules, and imperfect circular dichroism in monolayer *h*–BN, *Phys. Rev. Lett.* **128**, 047402 (2022).
- [32] B. Gil, G. Cassabois, R. Cusco, G. Fugallo, and L. Artus, Boron nitride for excitonics, nano photonics, and quantum technologies, *Nanophotonics* **9**, 3483 (2020).
- [33] Z. Li, G. Antonius, M. Wu, F. H. da Jornada, and S. G. Louie, Electron-phonon coupling from ab initio linear-response theory within the *GW* method: Correlation-enhanced interactions and superconductivity in $\text{Ba}_{1-x}\text{K}_x\text{BiO}_3$, *Phys. Rev. Lett.* **122**, 186402 (2019).
- [34] S. Dai, Z. Fei, Q. Ma, A. S. Rodin, M. Wagner, A. S. McLeod, M. K. Liu, W. Gannett, W. Regan, K. Watanabe, T. Taniguchi, M. Thiemens, G. Dominguez, A. H. Castro Neto, A. Zettl, F. Keilmann, P. Jarillo-Herrero, M. M. Fogler, and D. N. Basov, Tunable phonon polaritons in atomically thin van der waals crystals of boron nitride, *Science* **343**, 1125 (2014).
- [35] T. T. Tran, K. Bray, M. J. Ford, M. Toth, and I. Aharonovich, Quantum emission from hexagonal boron nitride monolayers, *Nat. Nanotechnol.* **11**, 37 (2016).
- [36] G. Cassabois, P. Valvin, and B. Gil, Hexagonal boron nitride is an indirect bandgap semiconductor, *Nat. Photonics* **10**, 262 (2016).
- [37] C. Elias, P. Valvin, T. Pelini, A. Summerfield, C. J. Mellor, T. S. Cheng, L. Eaves, C. T. Foxon, P. H. Beton, S. V. Novikov, B. Gil, and G. Cassabois, Direct band-gap crossover in epitaxial monolayer boron nitride, *Nat. Commun.* **10**, 2639 (2019).
- [38] M. M. Ugeda, A. J. Bradley, S.-F. Shi, F. H. da Jornada, Y. Zhang, D. Y. Qiu, W. Ruan, S.-K. Mo, Z. Hussain, Z.-X. Shen, F. Wang, S. G. Louie, and M. F. Crommie, Giant bandgap renormalization and excitonic effects in a monolayer transition metal dichalcogenide semiconductor, *Nat. Mater.* **13**, 1091 (2014).
- [39] T. Olsen, S. Latini, F. Rasmussen, and K. S. Thygesen, Simple screened hydrogen model of excitons in two-dimensional materials, *Phys. Rev. Lett.* **116**, 056401 (2016).
- [40] F. Paleari, T. Galvani, H. Amara, F. Ducastelle, A. Molina-S anchez, and L. Wirtz, Excitons in few-layer hexagonal boron nitride: Davydov splitting and surface localization, *2D Materials* **5**, 045017 (2018).
- [41] R. J. P. Rom an, F. J. C. Costa, A. Zobelli, C. Elias, P. Valvin, G. Cassabois, B. Gil, A. Summerfield, T. S. Cheng, C. J. Mellor, *et al.*, Band gap measurements of monolayer h-bn and insights into carbon-related point defects, *2D Mater.* **8**, 044001 (2021).
- [42] T. Hahn, S. Klimin, J. Tempere, J. T. Devreese, and C. Franchini, Diagrammatic monte carlo study of fr ohlich polaron dispersion in two and three dimensions, *Phys. Rev. B* **97**, 134305 (2018).
- [43] F. M. Peeters, W. Xiaoguang, and J. T. Devreese, Ground-state energy of a polaron in n dimensions, *Phys. Rev. B* **33**, 3926 (1986).
- [44] A. Ercelevi and G. S ualp, A variational treatment of a two-dimensional polaron, *J. Phys. Chem. Solids* **48**, 739 (1987).
- [45] R. Jalabert and S. Das Sarma, Quasiparticle properties of a coupled two-dimensional electron-phonon system, *Phys. Rev. B* **40**, 9723 (1989).
- [46] J. T. Titantah, C. Pierleoni, and S. Ciuchi, Free energy of the fr ohlich polaron in two and three dimensions, *Phys. Rev. Lett.* **87**, 206406 (2001).
- [47] K. Kaasbjerg, K. S. Thygesen, and K. W. Jacobsen, Phonon-limited mobility in *n*-type single-layer mos_2 from first principles, *Phys. Rev. B* **85**, 115317 (2012).

- [48] T. Sohler, M. Calandra, and F. Mauri, Two-dimensional fröhlich interaction in transition-metal dichalcogenide monolayers: Theoretical modeling and first-principles calculations, *Phys. Rev. B* **94**, 085415 (2016).
- [49] T. Deng, G. Wu, W. Shi, Z. M. Wong, J.-S. Wang, and S.-W. Yang, Ab initio dipolar electron-phonon interactions in two-dimensional materials, *Phys. Rev. B* **103**, 075410 (2021).
- [50] L. D. Landau, Electron motion in crystal lattices, *Phys. Z. Sowjet.* **3**, 664 (1933).
- [51] S. Pekar, Local quantum states of electrons in an ideal ion crystal, *Zh. Eksp. Teor. Fiz.* **16**, 341 (1946).
- [52] J. T. Devreese, Fröhlich polarons. Lecture course including detailed theoretical derivations, arXiv:1611.06122v5 (2020).
- [53] J. T. Devreese and A. S. Alexandrov, Fröhlich polaron and bipolaron: recent developments, *Rep. Prog. Phys.* **72**, 066501 (2009).
- [54] J. Spanier and K. B. Oldham, *An atlas of functions* (Taylor & Francis/Hemisphere, USA, 1987).
- [55] N. S. Rytova, Screened potential of a point charge in a thin film, *Proc. MSU, Phys. Astron.* **3**, 30 (1967).
- [56] L. V. Keldysh, Coulomb interaction in thin semiconductor and semimetal films, *JETP Lett* **29**, 658 (1979).
- [57] P. Cudazzo, I. V. Tokatly, and A. Rubio, Dielectric screening in two-dimensional insulators: Implications for excitonic and impurity states in graphane, *Phys. Rev. B* **84**, 085406 (2011).
- [58] The dimensionless function f appearing in Eq. (7) is $f(x) = x^2[x^6 - \pi x^5 + 28x^4 - 40\pi x^3 - 16(1 + 20 \log 2)x^2 + 240\pi x + 64(4 \log 2 - 7) + 64(5x^2 - 4) \log x]/(x^2 + 4)^4$.
- [59] R. P. Feynman, Slow electrons in a polar crystal, *Phys. Rev.* **97**, 660 (1955).
- [60] N. V. Prokof'ev and B. V. Svistunov, Polaron problem by diagrammatic quantum monte carlo, *Phys. Rev. Lett.* **81**, 2514 (1998).
- [61] T. Hahn, S. Klimin, J. Tempere, J. T. Devreese, and C. Franchini, Diagrammatic monte carlo study of fröhlich polaron dispersion in two and three dimensions, *Phys. Rev. B* **97**, 134305 (2018).
- [62] R. R. Nair, W. Ren, R. Jalil, I. Riaz, V. G. Kravets, L. Britnell, P. Blake, F. Schedin, A. S. Mayorov, S. Yuan, *et al.*, Fluorographene: a two-dimensional counterpart of teflon, *Small* **6**, 2877 (2010).
- [63] S.-J. Chang, S.-Y. Wang, Y.-C. Huang, J. H. Chih, Y.-T. Lai, Y.-W. Tsai, J.-M. Lin, C.-H. Chien, Y.-T. Tang, and C. Hu, van der waals epitaxy of 2d h-aln on tmds by atomic layer deposition at 250° c, *Appl. Phys. Lett.* **120**, 162102 (2022).
- [64] Z. Y. Al Balushi, K. Wang, R. K. Ghosh, R. A. Vilá, S. M. Eichfeld, J. D. Caldwell, X. Qin, Y.-C. Lin, P. A. DeSario, G. Stone, *et al.*, Two-dimensional gallium nitride realized via graphene encapsulation, *Nat. Mater.* **15**, 1166 (2016).
- [65] H. Zhang, M. Holbrook, F. Cheng, H. Nam, M. Liu, C.-R. Pan, D. West, S. Zhang, M.-Y. Chou, and C.-K. Shih, Epitaxial growth of two-dimensional insulator monolayer honeycomb BeO, *ACS Nano* **15**, 2497 (2021).
- [66] H. Wang, Y.-S. Lan, B. Dai, X.-W. Zhang, Z.-G. Wang, and N.-N. Ge, Improved thermoelectric performance of monolayer HfS₂ by strain engineering, *ACS Omega* **6**, 29820 (2021).
- [67] H. Y. Lv, W. J. Lu, D. F. Shao, H. Y. Lu, and Y. P. Sun, Strain-induced enhancement in the thermoelectric performance of a ZrS₂ monolayer, *J. Mater. Chem. C* **4**, 4538 (2016).
- [68] W. Li, S. Poncé, and F. Giustino, Dimensional crossover in the carrier mobility of two-dimensional semiconductors: the case of InSe, *Nano Lett.* **19**, 1774 (2019).
- [69] F. Ferreira, A. J. Chaves, N. M. R. Peres, and R. M. Ribeiro, Excitons in hexagonal boron nitride single-layer: a new platform for polaritonics in the ultraviolet, *J. Opt. Soc. Am. B* **36**, 674 (2019).
- [70] W. Zhang, Z. Huang, W. Zhang, and Y. Li, Two-dimensional semiconductors with possible high room temperature mobility, *Nano Res.* **7**, 1731 (2014).
- [71] A. Laturia, M. L. Van de Put, and W. G. Vandenberghe, Dielectric properties of hexagonal boron nitride and transition metal dichalcogenides: from monolayer to bulk, *npj 2D Mater. Appl.* **2** (2018).
- [72] N. A. Pike, A. Dewandre, B. Van Troeye, X. Gonze, and M. J. Verstraete, Vibrational and dielectric properties of the bulk transition metal dichalcogenides, *Phys. Rev. Materials* **2**, 063608 (2018).
- [73] W. Li and F. Giustino, Many-body renormalization of the electron effective mass of InSe, *Phys. Rev. B* **101**, 035201 (2020).
- [74] P. Garcia-Goiricelaya, J. Lafuente-Bartolome, I. G. Gurtubay, and A. Eiguren, Long-living carriers in a strong electron-phonon interacting two-dimensional doped semiconductor, *Commun. phys.* **2** (2019).
- [75] C. Yan, C. Gong, P. Wangyang, J. Chu, K. Hu, C. Li, X. Wang, X. Du, T. Zhai, Y. Li, and J. Xiong, 2D group IVB transition metal dichalcogenides, *Adv. Funct. Mater.* **28**, 1803305 (2018).
- [76] A. Alexandrov and J. Ranninger, Bipolaronic superconductivity, *Phys. Rev. B* **24**, 1164 (1981).
- [77] N. Mounet, M. Gibertini, P. Schwaller, D. Campi, A. Merkys, A. Marrazzo, T. Sohler, I. E. Castelli, A. Cepellotti, G. Pizzi, and N. Marzari, Two-dimensional materials from high-throughput computational exfoliation of experimentally known compounds, *Nat. Nanotechnol.* **13**, 246 (2018).
- [78] F. A. Rasmussen and K. S. Thygesen, Computational 2D materials database: electronic structure of transition-metal dichalcogenides and oxides, *J. Phys. Chem. C* **119**, 13169 (2015).

- [79] D. M. Ceperley and B. J. Alder, Ground state of the electron gas by a stochastic method, *Phys. Rev. Lett.* **45**, 566 (1980).
- [80] J. P. Perdew and A. Zunger, Self-interaction correction to density-functional approximations for many-electron systems, *Phys. Rev. B* **23**, 5048 (1981).
- [81] J. P. Perdew, K. Burke, and M. Ernzerhof, Generalized gradient approximation made simple, *Phys. Rev. Lett.* **77**, 3865 (1996).
- [82] D. R. Hamann, Optimized norm-conserving Vanderbilt pseudopotentials, *Phys. Rev. B* **88**, 085117 (2013).
- [83] M. Schlipf and F. Gygi, Optimization algorithm for the generation of ONCV pseudopotentials, *Comput. Phys. Commun.* **196**, 36 (2015).
- [84] K. Zhang, Y. Feng, F. Wang, Z. Yang, and J. Wang, Two dimensional hexagonal boron nitride (2D-hBN): synthesis, properties and applications, *J. Mater. Chem. C* **5**, 11992 (2017).
- [85] A. V. Lebedev, I. V. Lebedeva, A. A. Knizhnik, and A. M. Popov, Interlayer interaction and related properties of bilayer hexagonal boron nitride: *ab initio* study, *RSC Advances* **6**, 6423 (2016).
- [86] R. M. Ribeiro and N. M. R. Peres, Stability of boron nitride bilayers: Ground-state energies, interlayer distances, and tight-binding description, *Phys. Rev. B* **83**, 235312 (2011).
- [87] Q. Peng and S. De, Tunable band gaps of mono-layer hexagonal BNC heterostructures, *Physica E Low Dimens. Syst. Nanostruct.* **44**, 1662 (2012).
- [88] J. Qi, X. Qian, L. Qi, J. Feng, D. Shi, and J. Li, Strain-engineering of band gaps in piezoelectric boron nitride nanoribbons, *Nano Lett.* **12**, 1224 (2012).
- [89] R. J. Hunt, B. Monserrat, V. Zólyomi, and N. D. Drummond, Diffusion quantum Monte Carlo and *GW* study of the electronic properties of monolayer and bulk hexagonal boron nitride, *Phys. Rev. B* **101**, 205115 (2020).
- [90] M. Zhang, Y. Zhu, X. Wang, Q. Feng, S. Qiao, W. Wen, Y. Chen, M. Cui, J. Zhang, C. Cai, *et al.*, Controlled synthesis of ZrS₂ monolayer and few layers on hexagonal boron nitride, *J. Am. Chem. Soc.* **137**, 7051 (2015).
- [91] H. Şahin, M. Topsakal, and S. Ciraci, Structures of fluorinated graphene and their signatures, *Phys. Rev. B* **83**, 115432 (2011).
- [92] C. Verdi and F. Giustino, Fröhlich electron-phonon vertex from first principles, *Phys. Rev. Lett.* **115**, 176401 (2015).
- [93] J. Sjakste, N. Vast, M. Calandra, and F. Mauri, Wannier interpolation of the electron-phonon matrix elements in polar semiconductors: Polar-optical coupling in GaAs, *Phys. Rev. B* **92**, 054307 (2015).
- [94] F. Giustino, M. L. Cohen, and S. G. Louie, Electron-phonon interaction using Wannier functions, *Phys. Rev. B* **76**, 165108 (2007).
- [95] J. Lafuente-Bartolome, C. Lian, W. H. Sio, I. G. Gurtubay, A. Eiguren, and F. Giustino, Unified approach to polarons and phonon-induced band structure renormalization, *Phys. Rev. Lett.* **129**, 076402 (2022).
- [96] J. Lafuente-Bartolome, C. Lian, W. H. Sio, I. G. Gurtubay, A. Eiguren, and F. Giustino, Ab initio self-consistent many-body theory of polarons at all couplings, *Phys. Rev. B* **106**, 075119 (2022).
- [97] S. Kokott, S. V. Levchenko, P. Rinke, and M. Scheffler, First-principles supercell calculations of small polarons with proper account for long-range polarization effects, *New J. Phys.* **20**, 033023 (2018).
- [98] Z. Li, G. Antonius, M. Wu, F. H. da Jornada, and S. G. Louie, Electron-phonon coupling from *Ab Initio* linear-response theory within the *GW* method: Correlation-enhanced interactions and superconductivity in Ba_{1-x}K_xBiO₃, *Phys. Rev. Lett.* **122**, 186402 (2019).
- [99] H. Henck, D. Pierucci, G. Fugallo, J. Avila, G. Cassabois, Y. J. Dappe, M. G. Silly, C. Chen, B. Gil, M. Gatti, F. Sottile, F. Sirotti, M. C. Asensio, and A. Ouerghi, Direct observation of the band structure in bulk hexagonal boron nitride, *Phys. Rev. B* **95**, 085410 (2017).
- [100] R. Geick, C. H. Perry, and G. Rupprecht, Normal modes in hexagonal boron nitride, *Phys. Rev.* **146**, 543 (1966).
- [101] J. Heyd, G. E. Scuseria, and M. Ernzerhof, Hybrid functionals based on a screened coulomb potential, *J. Chem. Phys.* **118**, 8207 (2003).
- [102] C. Zhang, C. Gong, Y. Nie, K.-A. Min, C. Liang, Y. J. Oh, H. Zhang, W. Wang, S. Hong, L. Colombo, R. M. Wallace, and K. Cho, Systematic study of electronic structure and band alignment of monolayer transition metal dichalcogenides in van der waals heterostructures, *2d Mater.* **4**, 015026 (2016).
- [103] J. Sivek, O. Leenaerts, B. Partoens, and F. Peeters, First-principles investigation of bilayer fluorographene, *J. Phys. Chem. C* **116**, 19240 (2012).
- [104] Y. Ge, W. Wan, Y. Ren, F. Li, and Y. Liu, Phonon-limited electronic transport of two-dimensional ultrawide bandgap material h-BeO, *Appl. Phys. Lett.* **117**, 123101 (2020).
- [105] Y. Cai, Y. Liu, Y. Xie, Y. Zou, C. Gao, Y. Zhao, S. Liu, H. Xu, J. Shi, S. Guo, *et al.*, Band structure, effective mass, and carrier mobility of few-layer h-aln under layer and strain engineering, *APL Mater.* **8**, 021107 (2020).
- [106] Y. Jia, Z. Shi, W. Hou, H. Zang, K. Jiang, Y. Chen, S. Zhang, Z. Qi, T. Wu, X. Sun, *et al.*, Elimination of the internal electrostatic field in two-dimensional gan-based semiconductors, *npj 2D Mater. Appl.* **4**, 1 (2020).

- [107] B. Mortazavi, F. Shojaei, T. Rabczuk, and X. Zhuang, High tensile strength and thermal conductivity in beo monolayer: A first-principles study, *FlatChem* **28**, 100257 (2021).